

Highlights:

- 1) Simple coupled sea ice – ocean model has been developed to simulate the seasonal cycle of sea ice formation.
- 2) Salt flux associated with the wind-forced ice production causes haline convection affecting the characteristics of the entire water column.
- 3) The comparison between model-derived polynya extents and MODIS IST images was performed.
- 4) High resolution wind forcing is necessary to capture in more detail coastal sea ice processes, such as coastal polynyas, ice drift and ice compression against coastline features.

1 **Modelling sea ice formation in the Terra Nova Bay polynya**

2

3

4 Sansiviero M.¹, Morales Maqueda M. Á.^{2,3}, Fusco G.¹, Aulicino G.¹, Flocco D.⁴ and Budillon G.¹

5

6 ¹ Università degli Studi di Napoli “Parthenope” (Italy)

7 ² School of Marine Science and Technology, Newcastle University (United Kingdom)

8 ³ National Oceanography Centre (United Kingdom)

9 ⁴ Centre for Polar Observation and Modelling, University of Reading (United Kingdom)

10

11

12

13 Corresponding author: manuela.sansiviero@uniparthenope.it

14

15

16 **Abstract**

17 Antarctic sea ice is constantly exported from the shore by strong near surface winds that open leads
18 and large polynyas in the pack ice. The latter, known as wind-driven polynyas, are responsible for
19 significant water mass modification due to the high salt flux into the ocean associated with
20 enhanced ice growth. In this article, we focus on the wind-driven Terra Nova Bay (TNB) polynya,
21 in the western Ross Sea. Brine rejected during sea ice formation processes that occur in the TNB
22 polynya densifies the water column leading to the formation of the most characteristic water mass
23 of the Ross Sea, the High Salinity Shelf Water (HSSW). This water mass, in turn, takes part in the
24 formation of Antarctic Bottom Water (AABW), the densest water mass of the world ocean, which
25 plays a major role in the global meridional overturning circulation, thus affecting the global climate
26 system. A simple coupled sea ice – ocean model has been developed to simulate the seasonal cycle
27 of sea ice formation and export within a polynya. The sea ice model accounts for both thermal and
28 mechanical ice processes. The oceanic circulation is described by a one-and-a-half layer, reduced
29 gravity model. The domain resolution is $1\text{ km} \times 1\text{ km}$, which is sufficient to represent the salient
30 features of the coastline geometry, notably the Drygalski Ice Tongue. The model is forced by a
31 combination of Era Interim reanalysis and in-situ data from automatic weather stations, and also by
32 a climatological oceanic dataset developed from in situ hydrographic observations. The sensitivity
33 of the polynya to the atmospheric forcing is well reproduced by the model when atmospheric in situ
34 measurements are combined with reanalysis data. Merging the two datasets allows us to capture in
35 detail the strength and the spatial distribution of the katabatic winds that often drive the opening of
36 the polynya. The model resolves fairly accurately the sea ice drift and sea ice production rates in the
37 TNB polynya, leading to realistic polynya extent estimates. The model-derived polynya extent has
38 been validated by comparing the modelled sea ice concentration against MODIS high resolution
39 satellite images, confirming that the model is able to reproduce reasonably well the TNB polynya
40 evolution in terms of both shape and extent.

1. Introduction

Observations and models have clearly shown that changes in atmospheric forcing and ocean circulation affect the Antarctic sea ice extent (Jacobs and Comiso, 1997; Liu et al., 2004; Lefebvre et al., 2005; Zhang 2007; Turner et al., 2009; Liu and Curry, 2010). The pronounced pattern of increasing ice cover in the Ross Sea region, found to be the highest contributor to sea ice expansion amongst the five Southern Ocean sectors in the 1979 - 2010 period with a positive trend of $13700 \pm 1500 \text{ km}^2 \text{ yr}^{-1}$, has been ascribed to changes in atmospheric circulation (Parkinson and Cavalieri, 2012). Enhanced northward winds have changed sea ice drift and export offshore affecting the dynamics of the local oceanography. These changes impact on the occurrence of wind driven polynyas along the Antarctic coastal margin, modifying the production of dense water masses through sea ice growth (Holland and Kwok, 2012). Variation in size or extent of polynyas are believed to be suitable indicators of climatic change (Morales Maqueda et al., 2004).

The wind-driven Terra Nova Bay (TNB) polynya, located in the western sector of the Ross Sea, plays a major role in shaping the sea ice and ocean dynamics of this region (Kurtz and Bromwich, 1985; Bromwich, 1989). The polynya opening results principally from the synergy of meteorological, oceanographic, and physical geography features of this region (Fig.1). Especially during winter, the TNB polynya is frequently forced by cold and strong katabatic downslope flows that push sea ice away from the coast. Their action prevents sea ice from consolidating as a thick pack and, at the same time, facilitates its continuous formation by leaving the relatively warm open water exposed to the cold atmosphere. Also, the presence and the orientation of the Drygalski Ice Tongue is essential for the polynya maintenance, since this barrier blocks the incoming sea ice from the south and controls, through its length, the polynya extent (Frezzotti and Mabin, 1994). Due to the constant formation and offshore drift of new ice, the TNB polynya contributes significantly to the sea ice mass budget of the whole area, producing approximately 10% of the sea ice formed annually in the Ross Sea (Kurtz and Bromwich, 1985; Van Woert, 1999b). Associated with the wind-forced ice production is a salt flux that causes haline convection that affects the characteristics

67 of the entire water column in the TNB polynya and the thermohaline structure of the whole Ross
68 Sea (Kurtz and Bromwich, 1985; Trumbore et al., 1991). The TNB polynya is considered to be by
69 far the largest producer of High Salinity Shelf Water (HSSW) (Kurtz and Bromwich, 1983, 1985;
70 Jacobs et al., 1985; Van Woert, 1999a, b; Budillon and Spezie, 2000; Budillon et al., 2003; Fusco et
71 al., 2009), a water mass that plays a crucial role in the formation of Antarctic Bottom Water
72 (AABW) (Kurtz and Bromwich, 1985; Jacobs and Comiso, 1989; Van Woert, 1999a), thus
73 contributing to deep ocean ventilation and the global thermohaline circulation (Jacobs et al., 1985;
74 Orsi et al., 1999; Jacobs 2004).

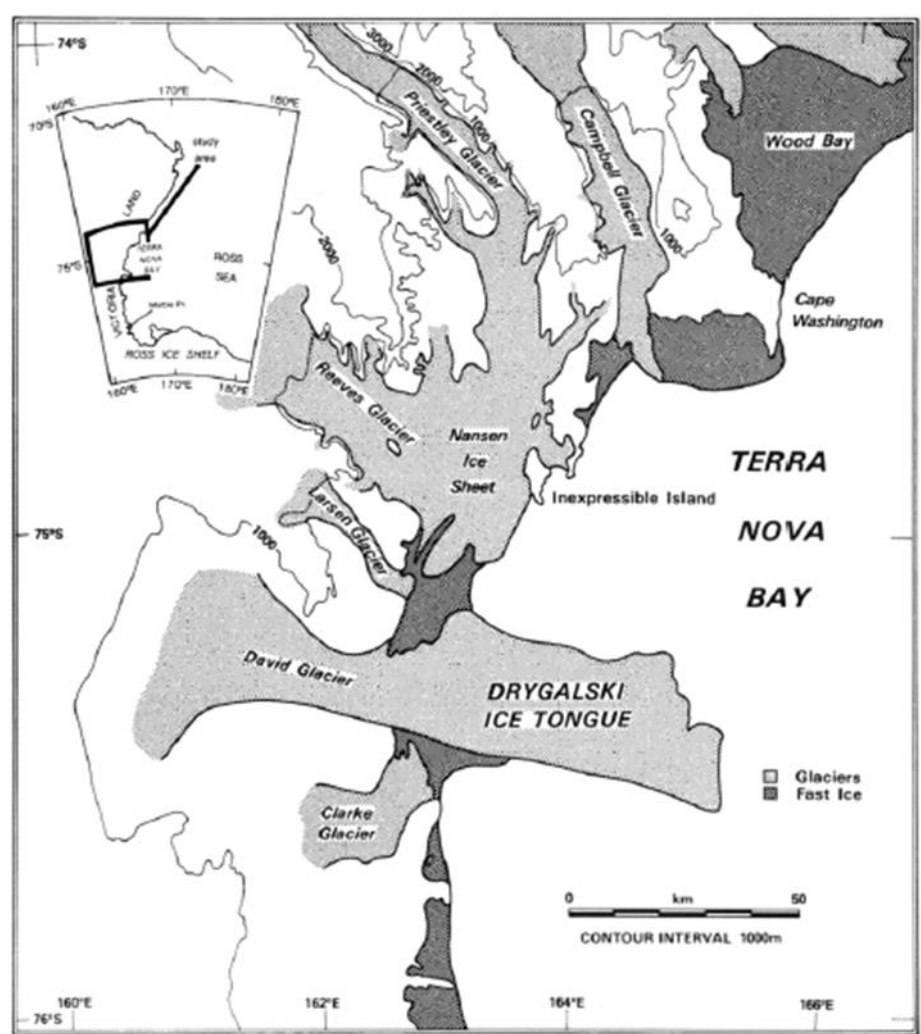


Fig. 1: Overview map of TNB (Western Ross Sea) showing the major geographical features of this region and its surroundings (Kurtz and Bromwich, 1983).

77 The main goal of this study is to investigate the sea ice behaviour in the Terra Nova Bay polynya in
78 response to external forcing and to estimate the associated sea ice and HSSW production. To this
79 purpose, a coupled sea ice – ocean model was developed and applied to the TNP polynya area. The
80 model simulates the seasonal cycle of sea ice formation in the TNB polynya, accounting for both
81 sea ice dynamic and thermodynamic processes. Dynamics does not produce ice directly, but causes
82 the ice to drift in and out of the area and leads to ice deformation in form of rafting or ridging due to
83 convergence. Thermodynamics processes are responsible for local ice growth or melt and heat
84 transfer at the ice-air and ice-ocean interfaces (Rothrock, 1979). Both ice dynamics and
85 thermodynamics alter the local mean thickness (ice volume per unit area) and result in the exchange
86 of mass, momentum and energy with the atmosphere and the ocean (Flato, 2003).

87 A further goal of this work is to estimate the variation of the TNB polynya extent, i.e. the size of the
88 area of low ice concentration, in response to the forcing. Computing the polynya extent is difficult
89 given the limitations of models and remote sensing tools as regards both their accuracy and their
90 ability to resolve polynya variability in space and time. Polynya extent estimates are not trivial to
91 derive since local ice thickness and ice production rates are often unknown. Papers focusing on the
92 variability of sea ice and open water in the TNB polynya exist in literature, mainly concerning the
93 wintertime season. Authors have investigated the TNB polynya extent either through one
94 dimensional models forced by in situ and reanalysis data (Van Woert, 1999a, 1999b; Fusco et al.,
95 2002; Petrelli et al., 2008) or through satellite observations (Kern, 2007; Ciappa et al., 2012).

96 The polynya extent in this paper is derived from modelled sea ice concentration and validated by
97 comparison with polynya extents estimates from MODIS satellite images (Key et al., 1994; Key et
98 al., 1997).

99 The paper is organized as follows. Section 2 provides a description of the coupled sea ice – ocean
100 model and the main formulations adopted to resolve sea ice dynamics and thermodynamics. Section
101 3 presents experiments on model sensitivity to variations in specific physical processes and
102 parameterizations in order to better tune the model to the peculiarities of the TNB polynya region.

103 In particular, the sea ice and polynya response to wind forcing variations is studied. Section 4 shows
 104 the results of a one year simulation of sea ice formation and polynya extent in the TNB polynya
 105 region. Section 5 focuses on the comparison between the numerical TNB polynya extent estimates
 106 and those derived from high resolution MODIS images. Finally, a discussion of results and a few
 107 concluding remarks are presented in Section 6.

108 **2. Description of the model**

109 **2.1 Model equations**

110 The coupled sea ice – ocean model presented here provides an intermediate complexity formulation
 111 of the TNB polynya dynamics. In contrast by polynya flux models describing the evolution of a
 112 polynya in terms of the polynya edge contour, our model predicts sea ice concentrations over a
 113 regular spatial grid (Willmott et al., 2007). The model has a relatively high resolution ($1 \text{ km} \times 1$
 114 km) in order to capture the complexity of the coastline geometry and the meteorological patterns of
 115 the region. Both dynamic and thermodynamic sea ice and ocean processes are incorporated in the
 116 model. An accurate representation of the main sea ice processes, often overlooked in numerical
 117 simulations of the polar regions (Russell et al., 2006; Maksym et al., 2012), and a realistic
 118 representation of sea ice dynamics, are crucial for the accurate description of the interactions of thin
 119 ice and polynyas with the atmospheric and oceanic circulation (Stössel et al, 1990). The ocean is
 120 represented by a one-and-a-half layer, reduced gravity, Boussinesq ocean model. The stratification
 121 is simplified using a description in which the active layer (effectively, the upper ocean mixed layer)
 122 moves above a lower stagnant (motionless) layer of infinite depth. The formulation of the ocean
 123 model is inspired in Morales Maqueda et al. (1999) and Biggs and Willmott (2001), with the only
 124 major departure that an eddy bolus transport term is added to the advection of scalars. The
 125 equations are as follows.

$$126 \quad h_1 \left(\frac{\partial U_1}{\partial t} + \frac{\partial(U_1 U_1)}{\partial x} + \frac{\partial(V_1 U_1)}{\partial y} \right) - f h_1 V_1 = - \frac{\partial}{\partial x} \left(\frac{1}{2} g \frac{\rho_r - \rho_1}{\rho_r} h_1^2 \right) + \frac{1}{\rho_r} (\tau_s^x - \tau_b^x), \quad (1)$$

$$h_1 \left(\frac{\partial V_1}{\partial t} + \frac{\partial(U_1 V_1)}{\partial x} + \frac{\partial(V_1 V_1)}{\partial y} \right) + f h_1 U_1 = - \frac{\partial}{\partial y} \left(\frac{1}{2} g \frac{\rho_r - \rho_1}{\rho_r} h_1^2 \right) + \frac{1}{\rho_r} (\tau_s^y - \tau_b^y), \quad (2)$$

$$\frac{\partial h_1}{\partial t} = - \left\{ \frac{\partial[h_1(U_1 + U_e)]}{\partial x} + \frac{\partial[h_1(V_1 + V_e)]}{\partial y} \right\} - E + P + M_s + M_i - G_i + w_b, \quad (3)$$

$$\frac{\partial(h_1 T_1)}{\partial t} = - \left\{ \frac{\partial[h_1 T_1(U_1 + V_e)]}{\partial x} + \frac{\partial[h_1 T_1(V_1 + V_e)]}{\partial y} \right\} + \frac{Q_1 + Q_i}{\rho_r c_p} + w_b T_b + h_1 \frac{T_c - T_1}{T_r}, \quad (4)$$

$$\frac{\partial(h_1 S_1)}{\partial t} = - \left\{ \frac{\partial[h_1 S_1(U_1 + U_e)]}{\partial x} + \frac{\partial[h_1 S_1(V_1 + V_e)]}{\partial y} \right\} + (M_i - G_i) S_i + w_b S_b + h_1 \frac{S_c - S_1}{T_r}. \quad (5)$$

131

132 In the equations above, h_1 is the depth of the ocean active layer, U_1 and V_1 are the x and y
 133 components of the ocean current in the active layer, \mathbf{U}_1 , f is the Coriolis parameter, g is the
 134 acceleration of gravity, ρ_r is a constant and uniform reference density representative on average of
 135 the densities encountered in the region below the active layer, ρ_1 is the density of the active layer,
 136 τ_s^x and τ_s^y are the components of the horizontal wind stress at the top of the active layer and,
 137 similarly, τ_b^x and τ_b^y are the components of the vertical shear stress at the bottom of the active layer,
 138 $U_e = -\kappa_e h_1^{-1} \partial h_1 / \partial x$ and $V_e = -\kappa_e h_1^{-1} \partial h_1 / \partial y$ are the components of the eddy bolus velocity
 139 (Gent and McWilliams, 1990), with κ_e a constant and uniform thickness diffusivity, E is
 140 evaporation, P is precipitation, M_s and M_i are the volume fluxes associated with snow and ice melt,
 141 respectively, G_i is ice growth (exception made of snow ice formation, which is described below),
 142 w_b represents the vertical volume flux at the base of the active layer caused by entrainment, T_1 is
 143 the temperature of the active layer, and Q_1 is the net surface heat flux into the layer, incorporating
 144 contributions from the ice free and ice covered areas and also including the latent heat loss required
 145 to melt the snow that falls over leads. Specifically,

$$Q_1 = (1 - A)(Q_{sw} + Q_{lw} + Q_s + Q_e - P L_f \rho_s) - A Q_c \quad (6)$$

147 where A is the fractional oceanic area covered by ice, or ice concentration, Q_{sw} , Q_{lw} , Q_s and Q_e are
 148 the shortwave, longwave, sensible and latent heat fluxes in the open ocean, the four quantities
 149 positive if they flow into the ocean and calculated according to Budillon et al. (2000), L_f is the
 150 latent heat of fusion of ice, ρ_s is snow density, and Q_c is the conductive heat flux through ice, which

151 we take as positive if directed upwards and assume to be identical to the heat flux from the ocean
 152 into the ice at the base of the ice cover. Small enthalpy changes associated with the mass fluxes E ,
 153 P , M_s , M_i and G_i are all ignored here since we neglect the thermal inertia of both snow and ice.
 154 Further in (4), Q_i is a latent heat flux associated with the formation or melting of ice in the active
 155 oceanic layer (see below) and T_b is the temperature associated with the volume flux w_b across the
 156 base of the active layer. The last term on the right hand side of (4) represents a relaxation to
 157 observations, T_c , with a time scale T_r . In (5), S_1 is the salinity of the active layer and S_i and S_b are
 158 the salinity of sea ice, which we take as constant and equal to 4, and the salinity of water entrained
 159 at the base of the active layer, respectively. Relaxation to salinity observations, S_c , is also included.
 160 The temperature T_1 is approximately maintained at the freezing point, T_f , which is calculated
 161 according to Fofonoff and Millard (1983), for as long as ice is present or if ice forms for the first
 162 time in the season in the open ocean. The term Q_i in (4) ensures this, and it has the form

$$163 \quad Q_i = \rho_r c_p \{ H(A) + [1 - H(A)] H(T_f - T_1) \} h_1 \frac{T_f - T_1}{T_i}. \quad (7)$$

164 In (7), H is the Heaviside function, A is the ice concentration, and T_i is a restoring time scale
 165 which we have chosen to be equal to the model time step. The entrainment velocity, w_b , depends on
 166 the air-sea stress and buoyancy fluxes that control the strength of turbulence in the mixed layer and
 167 is parameterized according to Lemke (1987) as

$$168 \quad w_b = \frac{2 u^{*3} e^{-h_1/h_w} + h_1 B [1 + H(B) (e^{-h_1/h_c} - 1)]}{g \frac{\rho_r - \rho_1}{\rho_r} h_1} \quad (8)$$

169 where $\rho_r u^{*2} = \sqrt{\tau_s^{x2} + \tau_s^{y2}}$, $h_w = 7 \text{ m}$, B is the surface buoyancy flux, and $h_c = 50 \text{ m}$. The
 170 temperature and salinity of entrained water, T_b and S_b , are determined using mooring based
 171 observations (see Section 2.3) linearly interpolated onto the bottom of the active layer.

172 The surface stress term is formulated as in Mellor and Kantha (1989) and is a linear combination of
 173 the shear stress at the surface of the ice covered ocean and the wind stress acting on the open ocean,
 174 weighted by the fractional area of sea ice and leads, respectively, namely, $\tau_s^x = (1 - A)\tau_{sw}^x + A\tau_{si}^x$,

175 where τ_{sw}^x is the x component of the surface stress over the ocean and τ_{si}^x is the sea ice counterpart.

176 An analogous equation holds for τ_s^y . In full, the ice-ocean stress components are

177
$$(\tau_{si}^x, \tau_{si}^y) = \rho_i C_i \sqrt{(U_1 - U_i)^2 + (V_1 - V_i)^2} (U_i - U_1, V_i - V_1), \quad (9)$$

178 where $C_i = 5 \times 10^{-3}$ is the ice-ocean drag coefficient, and U_i and V_i are the components of the ice
179 velocity. The stress at the base of the active layer is calculated according to the parameterization of
180 Pacanowski and Philander (1981):

181
$$(\tau_b^x, \tau_b^y) = \left(\nu_b + \frac{\nu_0}{(1 + \alpha Ri)^n} \right) \frac{1}{h_1} (U_1, V_1), \quad (10)$$

182 where $\nu_b = 1 \times 10^{-3} m^2 s^{-1}$, $\nu_0 = 1 \times 10^{-1} m^2 s^{-1}$, $\alpha = 0.5$, $n = 2$

183 and Ri is a Richardson number:

184
$$Ri = \frac{g \frac{\rho_r - \rho_1}{\rho_r} h_1}{u_1^2 + v_1^2}. \quad (11)$$

185

186 Sea ice behaves as a floating, zero layer system (i.e., without thermal inertia), as proposed by
187 Semtner (1976). Sea ice interacts thermodynamically and dynamically with the atmosphere and the
188 underlying mixed layer of the ocean. The coupling of sea ice with the surface ocean layer allows us
189 to simulate the seasonal cycle of sea ice formation and export within the polynya. The model
190 requires atmospheric and ocean forcing as inputs that are applied as surface and bottom boundary
191 conditions. The atmospheric forcing is given by air temperature, surface pressure, humidity, cloud
192 cover, precipitation and wind fields, from which surface heat, moisture and momentum fluxes can
193 be derived. The model needs also the solar radiation in order to compute the balance of radiative
194 and the turbulent heat fluxes. The ocean forcing consists of the ocean surface temperatures and
195 salinities. The main variables involved in the coupled sea ice-ocean model are shown in Fig. 2 as
196 well as a schematic decomposition of the heat balance at the air-ocean, air-ice and ice-ocean
197 interfaces.

198

199

$$S_A = (1 - A) \frac{Q_i / (L_f \rho_i)}{d}, \quad (15)$$

where, L_f is the latent heat of formation of ice, and, if $Q_i > 0$ (i.e., is there is frazil ice formation in the water column), d is a collection thickness of frazil ice which is either a constant or a function of wind speed as in Winsor and Bjork (2000), and we denote it by H , while, if $Q_i < 0$, $d = h_i$. The terms $\dot{V}_i = Q_i / (L_f \rho_i)$, \dot{V}_{i0} and \dot{V}_{si} in (13) account for ice growth/decay as a result of the heat budget in the active oceanic layer, for sea ice melting at the ice-atmosphere interface when the ice heat balance is such that the surface is at the melting point, and for snow ice formation, respectively. We note that the term G_i in (3) is simply equal to $H(\dot{V}_i)\dot{V}_i$. Snow ice formation occurs when the weight of snow depresses the snow-ice interface below sea level. In such cases, we transform the submerged snow into ice, leading to a contribution to the ice growth rate that obeys the formula

$$\dot{V}_{si} = \frac{A}{T_{si}} H \left(\frac{\rho_s h_s - (\rho_r - \rho_i) h_i}{\rho_r} \right) \frac{\rho_s}{\rho_i} \frac{\rho_s h_s - (\rho_r - \rho_i) h_i}{\rho_r}, \quad (16)$$

where T_{si} is a time scale that we take to be equal to the time step in the model. The term \dot{V}_{s0} in (14) accounts for both the accumulation of precipitating snow on top of sea ice and the subsequent surface snow melt during the thaw. As stated above, we make use of an approach for the sea ice and snow thermodynamics that is commonly termed zero layer approximation. This means that the vertical temperature profiles in the snow and the ice are linear and fully determined by the temperatures at their respective top and bottom interfaces. At the ice-ocean interface, the temperature is always taken to be T_f , and we further assume that the oceanic heat flux into the ice matches the conductive heat flux through the ice, Q_c , so that there is never a flux divergence at the bottom of the ice cover. At the ice-snow interface, the conductive heat flux is also assumed to be continuous. The conductive heat flux is given by the following expression (e.g., Fichefet and Morales Maqueda, 1997):

$$Q_c = \frac{\kappa_i}{h_i + \frac{\kappa_i}{\kappa_s} h_s} (T_f - T_0), \quad (17)$$

237 where κ_i and κ_s are the heat conductivities of ice and snow, respectively, and T_0 is the surface
 238 temperature. Finally, at the surface of the ice or snow cover a balance is postulated between surface
 239 and conductive heat fluxes, namely,

$$240 \quad Q_0 = Q_{swi} + Q_{lwi} + Q_{si} + Q_{ei} + Q_c = 0, \quad (18)$$

241 where Q_{swi} , Q_{lwi} , Q_{si} and Q_{ei} are the shortwave, longwave, sensible and latent heat fluxes at the
 242 surface of the snow or ice layer. The balance $Q_0 = 0$ in (18) can be guaranteed as long as T_0
 243 remains below the freezing point. However, if (18) requires that the surface temperature be above
 244 freezing then melting will ensure. During melting, T_0 will remain at the freezing point for
 245 freshwater (if snow is present) or for ice (if there is no snow) and the excess heat $Q_0 > 0$ will be
 246 used to melt snow, $M_s = Q_0 / (L_f \rho_s)$, or ice $M_i = Q_0 / (L_f \rho_i)$.

247 Sea ice drift, \mathbf{U}_i , with components U_i and V_i , is computed by postulating a balance of momentum
 248 between the Coriolis force, wind and ocean stresses and the ice internal force resulting from the
 249 interaction between floes during ice deformation. The momentum equations are:

$$250 \quad m \frac{\partial U_i}{\partial t} - f m V_i = A(\tau_w^x - \tau_o^x) + F^x, \quad (19)$$

$$251 \quad m \frac{\partial V_i}{\partial t} + f m U_i = A(\tau_w^y - \tau_o^y) + F^y, \quad (20)$$

252 where m is the mass of snow plus ice per unit area, τ_w^x and τ_w^y are the components of the wind stress
 253 acting on the ice, τ_o^x and τ_o^y are the components of the ice-ocean stress at the base of the ice, and
 254 F^x and F^y are the components of the ice internal stress force. Note that advection of sea ice
 255 momentum is ignored and that the atmosphere and ocean stresses term includes the ice
 256 concentration as a multiplicative factor to be consistent with the theory of free drift in regions of
 257 low ice concentration according to Connolley et al. (2004). The internal ice forces are resolved
 258 using the elastic-viscous-plastic rheology by Hunke and Dukowicz (1997). The internal ice pressure
 259 is formulated as a function of sea ice thickness, h_i , and concentration, A , as in Hibler (1979) (see
 260 further discussion in section 3.1).

261 **2.2 Model domain and set up**

262 The model domain consists of a wide region of the western Ross Sea including an extended area
263 along the coast of Victoria Land south of the Drygalski Ice Tongue and the northern region of the
264 Wood Bay (Fig. 3). It is $154 \text{ km} \times 488 \text{ km}$, extending approximately from 74°S to 78°S in latitude
265 and from 162°E to 168°E in longitude. A spatially uniform horizontal resolution of 1 km is used to
266 study the small scale behaviour of sea ice in TNB. This resolution is considered to be sufficient in
267 representing the salient features of the coastline geometry, such as the Drygalski Ice Tongue.
268 Hence, the horizontal grid is a rectangle of width X and length Y subdivided in square grid cells
269 resulting in a grid of $154 \times 488 = 75152$ grid points. An Arakawa B-grid is used for the spatial
270 discretization. A land mask is specified in the center of the cells with 0 representing land and 1
271 oceanic cells. A corresponding mask is defined for all corner quantities such as the wind speed, sea
272 ice velocity and stress components.

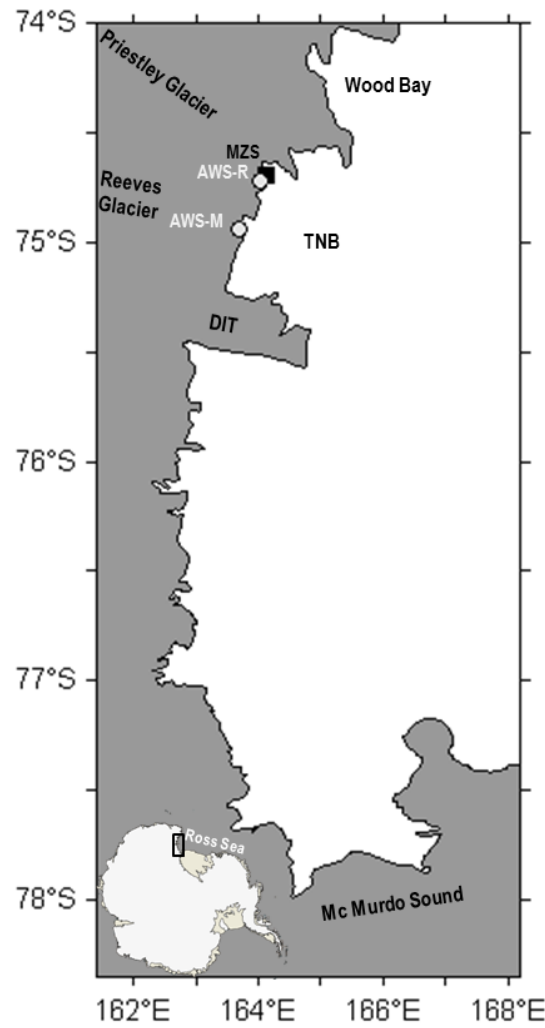


Fig. 3: The model domain showing the Drygalski Ice Tongue (DIT) and the two preferential paths of the katabatic flows, the Priestley and the Reeves Glaciers. The italian base, Mario Zucchelli Station (MZS), and the location of the automatic weather stations, Rita (AWS-R: 74.72°S, 164.03°E) and Manuela (AWS-M: 74.95°S, 163.69°E) are also indicated.

273

274

275 The advection of scalars is discretized with a first order upstream scheme. The solutions of the
 276 momentum equations (1), (2), (19) and (20) and the advective and thermodynamic processes in eqs.
 277 (3), (4), (5), (12), (13) and (14) are computed using two different time steps: a small one for the
 278 momentum (Δt) and a larger one for the advection (ΔT_a). All the input parameters such as constants
 279 and coefficients are shown in Table 1. Some values of the input parameters, referred to as “x” in
 280 Table 1, are let to vary in the sensitivity experiments. A one month spin-up length (repeated twice)
 281 is used for each experiment. Sea ice concentration and thickness and ocean fields are initialized at
 282 the beginning of each integration with a prescribed value or with a restart from a previous

283 integration. The initial values are zero for both ice concentration and thickness. The initial
284 temperature and salinity of the ocean are from monthly climatological observations (described in
285 section 2.3) and the initial active layer depth is determined from the former using the density
286 threshold criterion of 0.125 kg m^{-3} relative to near surface densities (Monterey and Levitus, 1997).
287 Open lateral boundary conditions ensuring a minimum of signal reflections at the boundary have
288 been used so that advective flows leaving the domain are allowed to freely exit the domain using an
289 upstream formulation, while flows into the domain use a simple sponge boundary condition that
290 relaxes the variables to their climatological external values (Martinsen and Engedahl, 1987). The
291 main physical parameters of atmosphere, sea ice and ocean used in the model are showed in Table
292 2. Figure 4 is the flow diagram of the coupled sea ice-ocean model, showing the basic steps in
293 computing the diagnostic variables of the model.

294

295	Parameter	Symbol	Value
	X domain	X	154000 m
	Y domain	Y	488000 m
296	T domain	T	x days
	Time step for momentum	Δt	1.2 s
	Time step for advection	Δt_a	600 s
297	Elastic timescale (EVP ice rheology)	Δt_e	180 s
	Air drag coefficient	C_{da}	x
	Ocean drag coefficient	C_{do}	x
298	Ice strength parameter	P^*	x N/m^2
	Ice concentration parameter	C	20
	Creep limit	c	$5 \times 10^{-11} \text{ 1/s}$
299	Eccentricity of the elliptical yield curve	e	2
	Ice collection thickness in leads	H	x m

300

301 **Table 1:** Input parameters of the model. The “x” stands for a varying value assigned to that parameter in the sensitivity experiments.

302

303

304

305

306

307

308

309

310

311

312

Parameter	Symbol	Value
Ocean eddy thickness diffusivity	K_e	$2 \times 10^2 \text{ m}^2 \text{ s}^{-1}$
Thermal conductivity of sea ice	κ_i	2.2 W/m/K
Thermal conductivity of snow	κ_s	0.3 W/m/K
Emissivity of atmosphere	ε_a	0.95
Emissivity of ocean	ε_o	0.985
Albedo of ocean	α_o	0.07
Albedo of ice	α_i	0.07-0.7
Albedo of snow	α_{sn}	0.85
Latent heat of fusion of ice	L_{fi}	$3.34 \times 10^5 \text{ J/kg}$
Latent heat of vaporization of water	L_e	$2.5 \times 10^6 \text{ J/kg}$
Latent heat of fusion of snow	L_{fsn}	$3.34 \times 10^5 \text{ J/kg}$
Latent heat of sublimation of snow	L_{ssn}	$2.834 \times 10^6 \text{ J/kg}$
Specific heat capacity of ocean	c_{pa}	3985 J/kg/K
Specific heat capacity of air	c_{pa}	1004 J/kg/K
Density of air	ρ_a	1.3 Kg/m ³
Density of ice	ρ_i	900 Kg/m ³
Density of snow	ρ_s	330 Kg/m ³
Density of ocean	ρ_o	1024 Kg/m ³
Melting point of freshwater ice	t_{fus}	0°C
Salinity of sea ice	s_i	4
Exchange coeff. for sensible heat (leads/ice)	c_H	1.75×10^{-3}
Exchange coeff. for latent heat over leads	c_E	1.75×10^{-3}
Exchange coeff. for latent heat over ice	c_E	1×10^{-3}
Stefan-Boltzmann constant	K	$5.67 \times 10^{-8} \text{ W m}^{-2} \text{ K}^{-4}$
Minimum vertical viscosity	v_{min}	$1 \times 10^{-3} \text{ m}^2 \text{ s}^{-1}$
Scale depth of mechanical dissipation	h_w	7 m
Scale depth of convective dissipation	h_c	50 m

Table 2: Physical parameters of atmosphere, sea ice and ocean.

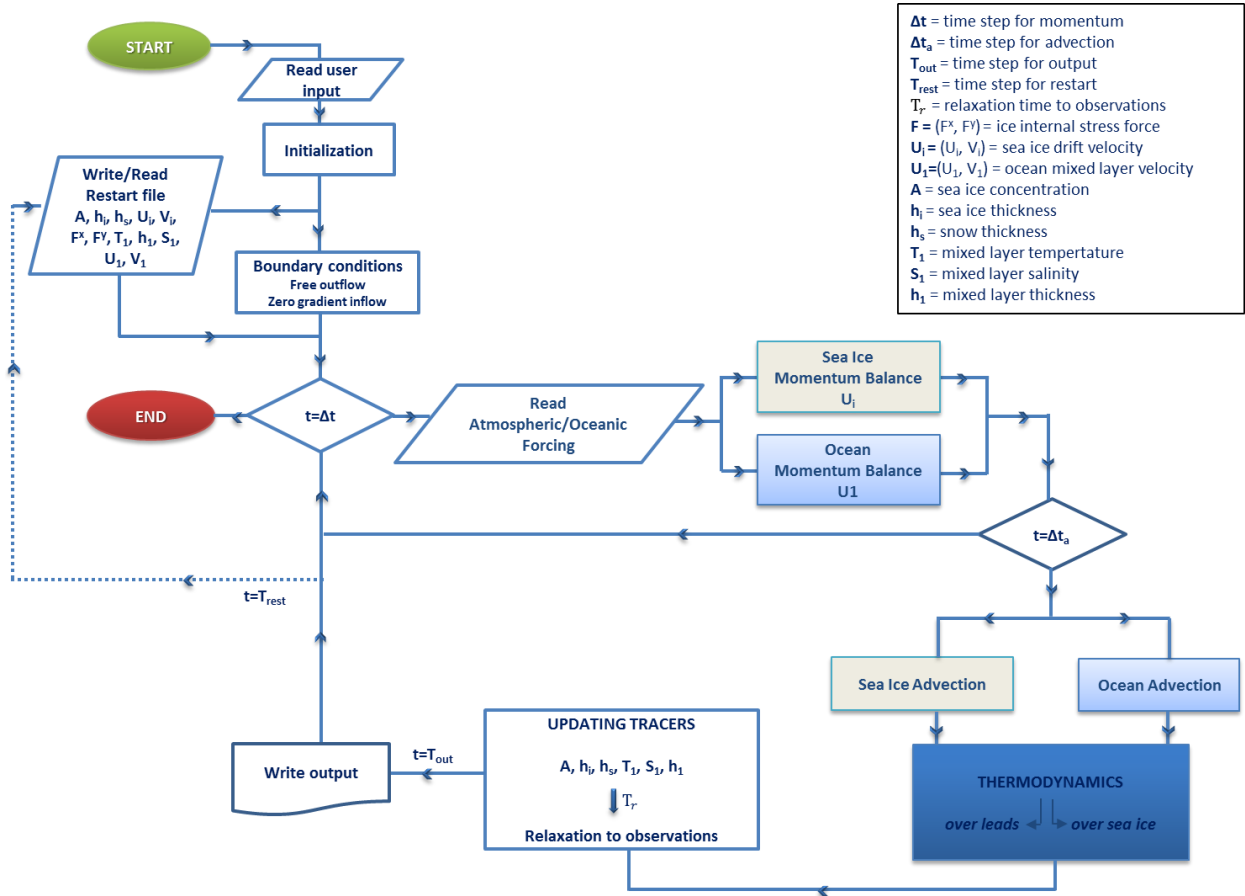


Fig. 4: Diagram flow of the coupled sea ice - ocean model.

327 **2.3 Forcing Fields**

328 The ocean forcing consists of climatological oceanographic profiles of ocean temperature and
329 salinity developed through the analysis of available in situ temperature and salinity datasets. These
330 datasets consist of hydrographic mooring and CTD profile data collected from February 1995 to
331 January 2008 within the CLIMA (Climatic Long-term Interaction for the Mass-balance in
332 Antarctica) project of the Italian National Research Antarctic Program (PNRA). The two
333 climatological datasets include idealized monthly temperature and salinity values, spatially uniform
334 in the model domain and varying vertically down to 800 meters in depth. In detail, 8 depth levels (0
335 m, -30 m, -50 m, -100 m, -150 m, -300 m, -500 m, -800 m) are chosen for the computation of
336 climatological temperature and salinity profiles (see Section 2.3) that are subsequently used to
337 calculate, by linear interpolation, the temperature, T_b , and salinity, S_b , at the base of the active layer
338 as well as the restoring temperature, T_c , and salinity, S_c , in the active layer. As main atmospheric
339 forcing, the Era-Interim reanalysis from the European Centre for Medium-Range Weather Forecasts
340 (ECMWF), has been prescribed. The data extracted from the global domain provide surface six-
341 hourly parameters at a 0.5×0.5 degree horizontal resolution covering the model domain with $16 \times$
342 11 grid points, in latitude \times longitude. Specifically, the input data consist of the 10 meter eastward
343 and northward wind components (m/s), the 2 meter temperature (K), the downward surface solar
344 radiation (Wm^{-2} s), the surface (1000 mb level) pressure (Pa), the relative humidity (%), the total
345 cloud cover (0-1) and the total precipitation accumulation (m of water). The oceanographic and
346 atmospheric data have been spatially and temporally interpolated over the whole model domain.
347 Meteorological observations from Automatic Weather Stations (AWSs) have also been employed
348 to force the model.

349

350

351 2.3.1 Atmospheric field setting

352

353 The resolution of the local winds is a crucial factor in estimating sea ice and HSSW production,
354 especially in a small coastal polynya like the TNB. In particular during winter, sea ice production in
355 TNB is largely determined by katabatic winds which are the main control of the TNB polynya size
356 (Petrelli et al., 2008; Gallé, 1997). Petrelli et al. (2008) showed that an insufficient resolution of the
357 katabatic winds leads to an underestimation of sea ice winter production of up to 50%, which results
358 in an underestimation of the formation rate of HSSW and consequently of AABW. On the other
359 hand, low resolution winds reanalyses can also result in higher ice and AABW production because
360 of an overestimated offshore component due to the coarse resolution orography (Stössel et al.,
361 2011).

362 In spite of their relatively high resolution, the ECMWF reanalysis have been found to underestimate
363 the wind speeds in several studies (Cullather et al., 1997; Fusco et al., 2002; Petrelli et al., 2008),
364 providing therefore an improper representation of the wind fields along and offshore TNB. Also
365 Mathiot et al. (2010) investigated the effect of the katabatic winds on sea ice and shelf water
366 properties by correcting the ECMWF reanalyses winds with results from the MAR regional
367 atmospheric model. To remedy this problem, we have applied a wind correction to coastal and
368 offshore model grid points value combining the Era Interim data with in-situ atmospheric data from
369 Automatic Weather Stations (AWSs), which show a significantly increased skill over ECMWF
370 atmospheric variables (Petrelli et al., 2008).

371 A merging function has been designed so that the correction factor for each grid point value varies
372 with the distance from the weather station. Era Interim and AWS data are merged resulting in the
373 effective wind vector defined as

$$374 V_{eff} = V_{AWS} e^{-\frac{r}{R}} + V_{Era} \left(1 - e^{-\frac{r}{R}}\right), \quad (21)$$

375 where V_{AWS} and V_{Era} are the wind vectors from AWS and ERA-Interim, respectively, r is the
376 distance from the AWS and R is an e-folding length scale.

377 In particular, atmospheric data from two AWSs have been used. In a first phase of the sensitivity
378 tests, only the Rita AWS (-74.72° S, 164.03° E), installed within the Meteo-Climatological
379 Observatory of the PNRA in close proximity to the Italian base “Mario Zucchelli”, downstream of
380 the Priestley Glacier (Fig. 3), has been considered.

381 Subsequently, the Manuela AWS (-74.95° S, 163.69° E), installed as part of the AWS project of
382 the University of Wisconsin-Madison Antarctic Meteorology Program on Inexpressible Island, has
383 been also included. The AWS Manuela lies downstream of the Reeves Glacier (Fig. 3), which
384 represents one of the main route for the katabatic flows from the interior of Antarctica.

385 The Rita and Manuela datasets consist, respectively, of one hourly and ten minute intervals data
386 including air temperature ($^{\circ}$ C), wind speed (m/s) and direction ($^{\circ}$ N), surface pressure (hPa), and
387 relative humidity (%). The merging function (21) has been applied also to the air temperature and
388 relative humidity data.

389

390 **3 Sensitivity experiments**

391 An improper choice of the parameters which describe sea ice evolution results often in unrealistic
392 simulations leading to inaccurate results. Several sensitivity experiments were performed to define
393 the best set of parameters controlling TNB sea ice dynamics and thermodynamics in response to
394 wind forcing. Two key parameters have been found to control the wind driven polynyas: the
395 rheological ice strength parameter P^* and the demarcation ice collection thickness H , also named
396 the lead-closing parameter. The rate at which the leads close under freezing conditions is inversely
397 proportional to the value of H . Both parameters have a strong effect on polynya size and sea ice
398 extent and volume estimates (Hibler, 1979; Stössel et al., 1990; Stössel, 1992).

399 Finally a sensitivity analysis was carried out turning attention to the air-ice and ice-ocean drag
400 coefficients which control the stresses on the sea ice cover. The choice of these parameters depends

on the study area and especially on the wind forcing time and spatial resolution, therefore the model was opportunely tuned and optimized in this regard.

3.1 Sensitivity to ice strength parameter

The ice strength parameter P^* is a key element in sea ice rheology that relates sea ice strength (P) to its concentration, A , and mean thickness, Ah_i . It was first introduced by Hibler (1979) in the constitutive equation for sea ice strength as

$$P = P^* Ah_i \exp [-C(1 - A)] \quad (22)$$

where P^* and C are empirical values. The ice strength exhibits a strong dependence on sea ice concentration and especially on the amount of thin ice. For a large amount of thin ice, the ice strength decreases significantly and most of thin ice is deformed (Hibler, 1979; Willmott et al., 2007; Feltham, 2008). Sea ice also offers less resistance to compression when Ah_i and P^* are low, and tends to pile up more easily because of enhanced mechanical ridging and rafting. Therefore, P^* is a critical parameter controlling sea ice drift behaviour in wind driven polynyas and represents the main tuning parameter to achieve a realistic sea ice drift pattern (Owens and Lemke, 1990; Stössel et al., 1990; Steele et al., 1997).

The strength of the ice internal forces depends on the state of deformation of the sea ice cover, which will, in turn be partly controlled by the wind stress field. Based on this observation, we have carried out a series of sensitivity experiments to investigate the impact on the ice dynamics of varying P^* and introducing the katabatic wind parameterisation given by (21). Table 3 displays the different combinations of P^* and wind merging parameter R in four experiments. The control experiment, referred to as CASE 1, uses a $P^* = 27500 \times 10^4 \text{ N/m}^2$, as in Hibler and Walsh (1982), which is the most widely used value for the ice strength parameter, and $R=25 \text{ km}$. CASE 2 is different from the control run just for $P^* = 5000 \text{ N/m}^2$, as in Hibler (1979), while CASE 3 and

CASE 4 differ from the control experiment in the absence of the merging between reanalyses and AWS data and in the larger influence range of AWS data, respectively.

427

Experiment	P^* (N/m ²)	R (km)
CASE 1	27500	25
CASE 2	5000	25
CASE 3	27500	-
CASE 4	27500	50

Table3: Sensitivity tests of sea ice evolution with respect to P^* and R factor.

432

In all the runs the demarcation ice collection thickness, H , was set to 0.1 m. Regarding the oceanic forcing, a relaxation time of $T_r = 7$ days to climatological data was set in all the experiments. The time interval of the atmospheric input was set to 6 hours, while that of the output fields is such that the model gives a daily output for each computed variable. Figures 5 (a, b e c) depict the wind, sea ice drift and ocean fields on 8th July 2000. CASE 1 and CASE 2 use the same wind field and so one wind velocity panel is shown for both of them in figure 5. The wind velocities have maximum values of 19.66 m/s in CASE 1/CASE 2 and 20.65 m/s in CASE 4, while in CASE 3, where the merging function is switched off, they reach a maximum value of only 7.27 m/s. The ice velocities show max values of 0.32-0.34 m/s and mean values of 0.05-0.08 except in CASE 3, where the ice drift is forced only by the ERA-Interim data, showing smaller max and mean values of 0.1 m/s and 0.03 m/s respectively. The reduced ice strength does not affect significantly the ridging of sea ice or the sea ice drift in convergent regions, altering relatively little the ice concentration and thickness distribution (not shown). This indicates the polynya area is not highly sensitive to P^* in the determination of its opening/closure for this set of forcing.

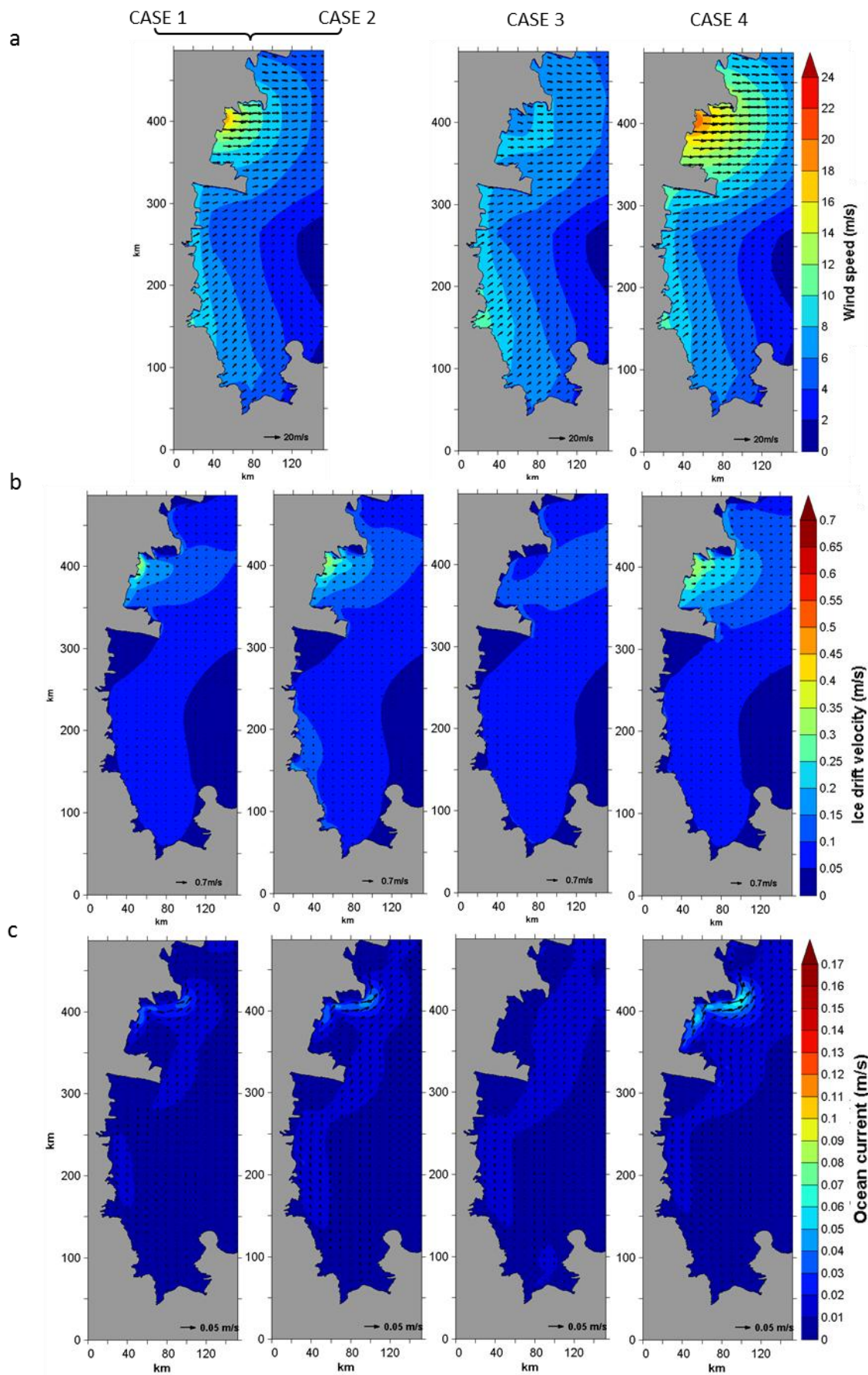


Fig. 5: Maps of wind speed (a), modelled ice drift velocity (b) and modelled ocean current (c) overlaid by the corresponding wind speed vectors, ice drift velocity vectors and ocean current vectors on 8th July 2000 for CASE 1 to CASE 4.

448 This is probably due to the fact that this parameter has a major influence only in areas of thick ice
449 but rather not so much in regions covered by thin and broken ice cover (Kreysner et al., 2000). In
450 contrast, an increasing of the R factor (CASE 4) leads, as expected, to larger ice drift velocities and
451 hence to a greater polynya extent.

452

453 **3.2 Sensitivity to demarcation ice collection thickness**

454 While the dynamic behaviour of the consolidated ice is greatly determined by the ice rheology, the
455 interior of the polynya is affected by the new ice thickness parameterization. The new ice thickness
456 is controlled by the demarcation ice collection thickness parameter H in eq. (15) that is expressed as
457 a transition value between thin ice (open water) and thick ice (Hibler, 1979). It is as crucial an
458 element in sea ice models as the ice thickness collection depth in polynya flux models (Tear et al.,
459 2003; Willmott et al., 2007) since it represents the thickness at which newly-formed ice in the
460 polynya is transferred into thicker solid sea ice. Thereby, it affects sea ice thermodynamics,
461 lowering heat loss through thin ice inside the polynya and determining primarily the mean thickness
462 and sea ice concentration of newly formed ice (Hibler, 1979; Olason and Harms, 2010).

463 H has been often defined as a constant in the literature, with typical values in the range 0.1-0.5 m
464 (Hibler, 1979; Pease, 1987; Ou, 1988; Darby et al. 1994, 1995). However, wind speed is an
465 important controlling factor of the collection thickness of new ice (Mellor and Kantha, 1989;
466 Winsor and Björk, 2000; Olason and Harms, 2010).

467 A number of experiments, outlined in Table 4, were performed with different values of H . The
468 control experiment (CASE 5) was run with $H=0.2$ m, that is considered more appropriate than the
469 $H=0.5$ m proposed by Hibler (1979), in simulating the behaviour of thin ice inside the polynya
470 (Olason and Harms, 2010). In the second (CASE 6) and third experiment (CASE 7), sea ice
471 concentration and thickness are simulated using a constant $H=0.3$ m and $H=0.4$ m respectively,

472 while in the fourth experiment (CASE 8) a varying H has been used. Specifically, the collection
 473 depth parameterization of Winsor & Björk (2000) is employed, namely,

474
$$H = \frac{a + V \cdot b}{c}, \tag{23}$$

475 where V is the surface wind speed (m/s) and the constants are $a = 1$ m, $b = 0.1$ s and $c = 15$. This
 476 means that H varies in the range 0.1-0.3 m in the presence of wind speeds between 5-35 m/s.

477 In all these experiments, R is fixed to 50 km, except in CASE 9, in which the merging function is
 478 not applied. The value of 27500 N/m² for P^* and of 30 days for the relaxation time to oceanic
 479 forcing were used. Figure 6 shows the results of sea ice concentration (a) and thickness (b)
 480 simulation on 8th July 2000 for CASE 5–to–CASE 9. Note that a lower ice demarcation thickness
 481 gives higher ice concentration values and lower ice thickness values due to lower heat losses
 482 through leads.

483

Experiment	H (m)	R factor (km)
CASE 5	0.2	50
CASE 6	0.3	50
CASE 7	0.4	50
CASE 8	f (V)	50
CASE 9	0.2	-

486 **Table 4:** Sensitivity tests of sea ice evolution with respect to H and R factor.

487

488

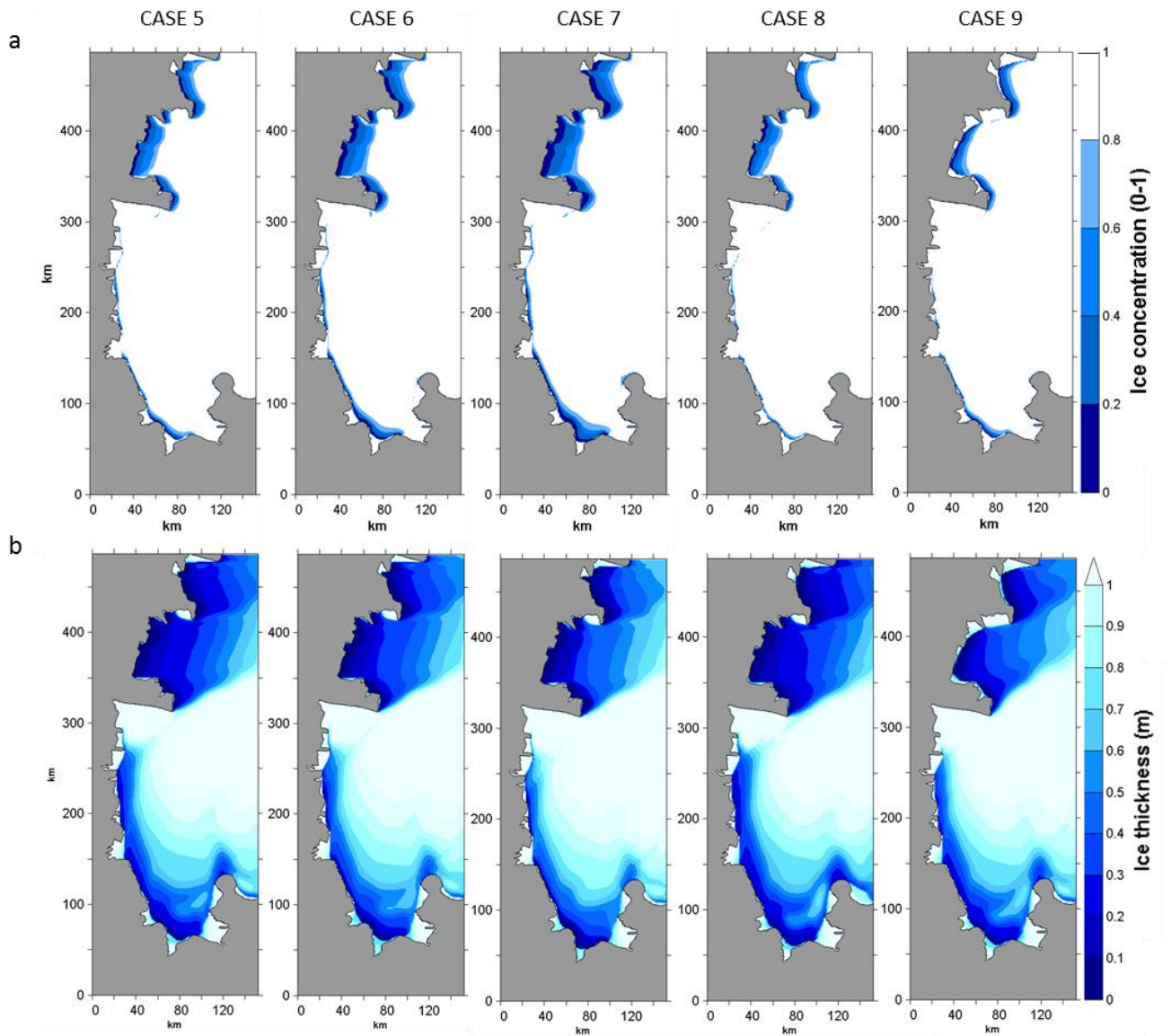


Fig. 6: Maps of modelled sea ice concentration (a) and thickness (b) on 8th July 2000 for CASE 5, CASE 6, CASE 7, CASE 8 and CASE 9.

489

490 The sea ice distribution in CASE 8 is similar to that of CASE 5, suggesting that the dependence of
 491 the ice collection thickness on the wind velocities provides plausible values for H . This is well
 492 supported by the estimates of daily sea ice production (km^3/day) in TNB region on July 2000 (Fig.
 493 7). Cumulative sea ice production (km^3) for the whole of July 2000 is also showed in Table 5. Note
 494 that the TNB region is identified by the area of the domain that extends within the ranges 1-120 km
 495 in X (longitude) and 310-425 km in Y (latitude) as shown in figure 7. Sea ice production rate
 496 computed using a non-spatially uniform H (CASE 8) depicted by the solid line with square markers

497 shows a trend very similar to that of CASE 5, except for a few days when wind speeds in the
 498 polynya were particularly large. As it can easily be observed, CASE 9, where wind forcing is given
 499 by the winds reanalysis alone, underestimates considerably sea ice production rate compared to
 500 CASE 5 and, indeed, all the others. These results suggest reasonable agreement between the wind
 501 forcing and the simulated sea ice dynamics in the TNB.
 502 In the next section we will consider the sensitivity of the TNB polynya to the wind forcing and
 503 wind stress (Stössel, 1992; Stössel et al., 2011) pointing out the importance of high temporal
 504 resolution of wind data.

505

Experiment	Sea ice production (km ³) in July 2000
CASE 5	10.08
CASE 6	11.09
CASE 7	12.12
CASE 8	9.79
CASE 9	6.83

506

509 **Table 5:** Sea ice production in July 2000 for the experiments CASE 5 to CASE 9.

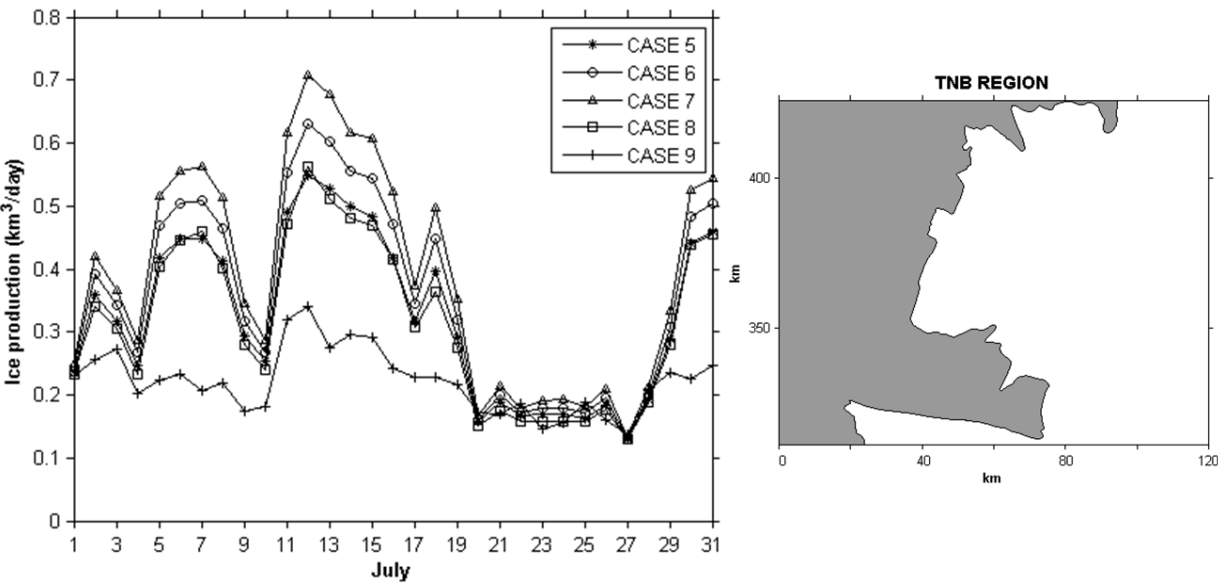


Fig. 7: Daily ice production (left) on July 2000 for CASE 5 to CASE 9 within a smaller area of the domain, defined as TNB region (right), extending approximately from 310 km to 425 km in Y and bordered by X = 120 km.

510

511

512 3.3 Sensitivity to air-ice and ice-ocean drag coefficients

513 Along with P^* , the atmospheric and oceanic drag coefficients have been identified as crucial
514 parameters for sea ice drift. Several sensitivity experiments were performed to obtain the optimal
515 set of drag coefficients that would allow us to run the model under more realistic conditions.

516 We also focused on the regime of the katabatic winds and its impact on sea ice evolution in the
517 TNB and on the polynya size. The latter, in fact, is very responsive to variations in the freezing
518 rates in the bay as a result of a weakening of the katabatic flows or a change in their direction
519 (Bromwich and Kurtz, 1984; Priestley, 1914). The duration of the katabatic wind events has a
520 greater contribution than the intensity and frequency of the katabatic flows in determining the
521 polynya extent (Ciappa et al., 2012; Rusciano et al., 2013). Rusciano et al. (2013) found most
522 frequent katabatic events take place during the winter season and last on average from one to three
523 hours. That means that long time intervals (daily/six hourly) atmospheric input probably
524 misrepresent the real and local atmospheric fields in a given temporal period. On the other hand, a
525 single source of AWS data fails to properly reproduce the geometry of the coastal wind regime
526 resulting from the drainage of the interior katabatic airflows through the different confluence
527 pathways (Petrelli et al., 2008). In view of these considerations, in the next experiments, the time
528 resolution was increased so that the model is able to capture any katabatic events. Furthermore, a
529 second dataset from AWS Manuela (see section 2.3.1) was taken into account to enlarge the area of
530 influence of the katabatic flows. Unfortunately, no other weather station is available in the
531 southernmost region of the bay and near to the Drygalski Ice Tongue. In addition, the merging
532 function was modified and the range of influence of the AWS data on the reanalysis data was let to
533 assume an elliptic shape rather than a circumference as follows:

$$534 \quad V_{eff} = V_{AWS} e^{-\sqrt{\frac{x^2}{R_1^2} + \frac{y^2}{R_2^2}}} + V_{Era} \left(1 - e^{-\sqrt{\frac{x^2}{R_1^2} + \frac{y^2}{R_2^2}}} \right), \quad (24)$$

535 where x and y are the components of the position vector of a particular point in the domain with
536 respect to the AWS, and $R_1 = 50$ km and $R_2 = 20$ km are e-folding length scales in the x and y
537 directions. Table 6 summarises the experiments performed to explore the impact of varying the C_{da}
538 and C_{do} drag coefficients, increasing and/or decreasing the one with respect to the other, on sea ice
539 drift and polynya dynamics. Substantially, an increasing of C_{da} and/or at the same time a decreasing
540 of C_{do} allows sea ice to move faster and vice versa. We have made use of a double sub-index to
541 identify easily the wind and ocean drag coefficients used in a particular experiment, e.g. the
542 experiment denoted by E_{ab} uses $C_{da} = a \times 10^{-3}$ and $C_{do} = b \times 10^{-3}$.

543 The first experiment (E_{15}) is the control simulation of one winter month of the year 2005 for which
544 the model has been configured with constant and more commonly used values for the drag
545 coefficients, $C_{da} = 1 \times 10^{-3}$ and $C_{do} = 5 \times 10^{-3}$. In the next experiments, the values of the two drag
546 coefficients were allowed to vary individually or simultaneously with respect to those of the control
547 run. Specifically, in the second experiment (E_{35}) C_{da} varies and C_{do} is the same as in the control
548 run, in the third experiment (E_{11}), only C_{do} varies, while, in the fourth (E_{31}) and in the fifth (E_{34})
549 experiments, both parameters vary together. The sixth experiment (E_r), which is in more detail
550 described afterwards, was carried out using non constant values for the drag coefficients. All the
551 experiments are forced with atmospheric forcing from the AWS Manuela at ten minutes resolution,
552 combined with hourly data from the AWS Rita. The resulting values are averaged with the six
553 hourly ERA-Interim data so as to adjust the background atmospheric fields, especially the winds. In
554 addition, the output time of the variables simulated by the model were set equal to 3 hours since, as
555 explained above, this value would appear to be a good compromise to capture the effects of
556 katabatic winds.

557 As the sensitivity experiments described in previous sections, a significant dependence of the sea
558 ice simulation on the wind forcing can be inferred from the results of the modelled output fields.
559 The sea ice distribution appears to be very sensitive to the pattern of the wind stress which varies
560 considerably depending on the surface winds. Fig. 8 (a) shows the wind speeds and the wind stress

vector fields for the E₁₅, E₃₅, E₁₁, E₃₁ and E₃₄. The wind field is the same for all the experiments since they have been forced with the same wind configuration, which has maximum wind speed values of up to 23 m/s and a mean value of 9 m/s. The wind stress, depending on the drag parameters, exhibits average values of 0.16, 0.41, 0.13, 0.27 and 0.40 N/m² in E₁₅, E₃₅, E₁₁, E₃₁, E₃₄, respectively. The largest values have been found, as expected, in E₃₅, E₃₁ and E₃₄ with maxima of 1.48, 1.34 and 1.47 N/m² versus much smaller maxima in the CTRL run (E₁₅) and in E₁₁ of approximately 0.54 N/m².

Experiment	C_{da}	C_{do}
E ₁₅ <u>CTRL</u>	1×10^{-3}	5×10^{-3}
E ₃₅	3×10^{-3}	5×10^{-3}
E ₁₁	1×10^{-3}	1×10^{-3}
E ₃₁	3×10^{-3}	1×10^{-3}
E ₃₄	3×10^{-3}	4×10^{-3}
E _r	1×10^{-3} $V \leq 10$ m/s 3×10^{-3} $V \geq 20$ m/s	$1.3 \times C_{da}$

Table 6: Sensitivity tests with respect to the air-ice and ice-ocean drag coefficients. The double sub-index identifies the wind and ocean drag coefficients used in each experiment.

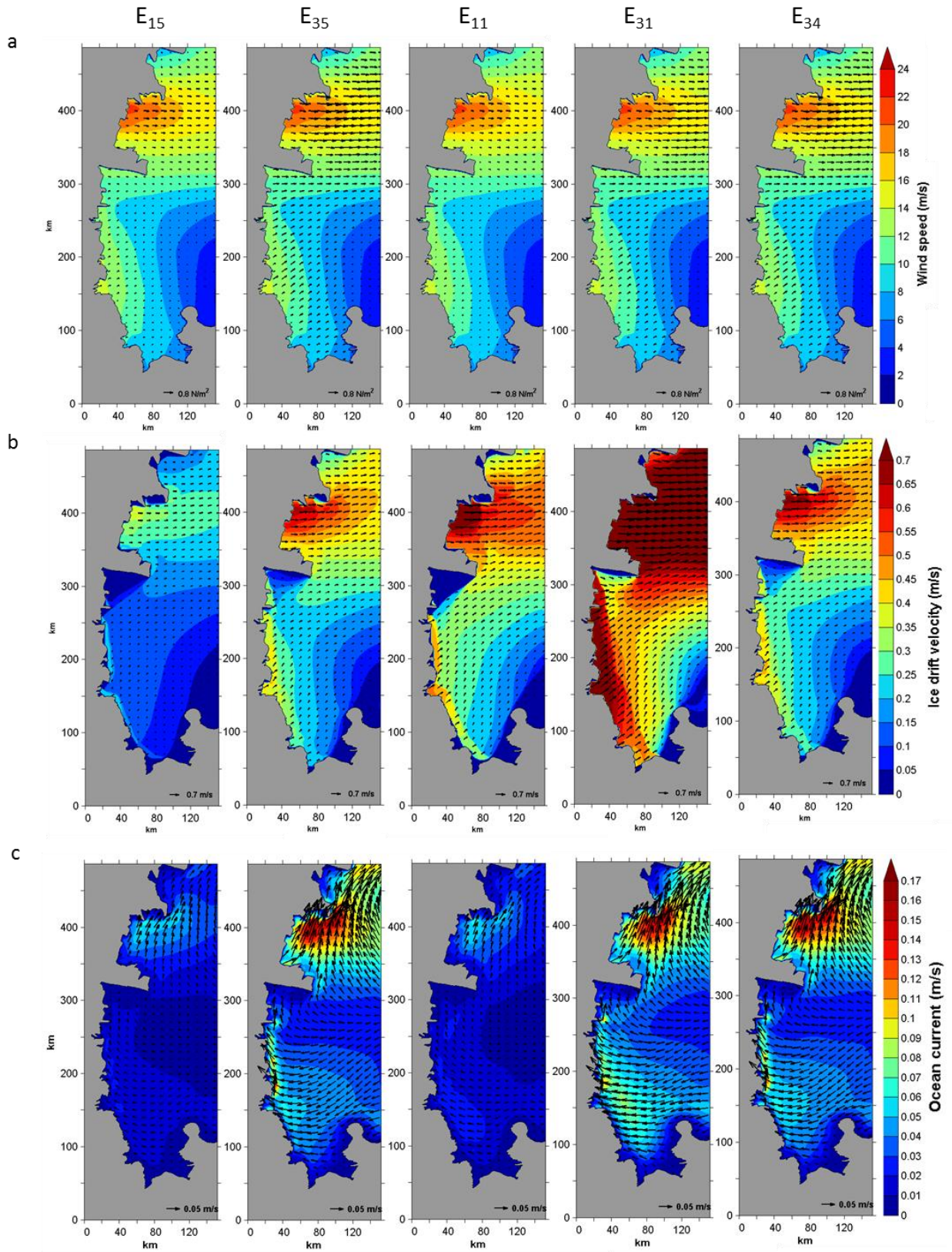


Fig. 8: Wind speeds (a), sea ice drift velocities (b) and ocean currents (c) with the superimposed wind stress, ice drift and ocean current vectors, respectively on 30th July 2005 for E₁₅, E₃₅, E₁₁, E₃₁, E₃₄.

580 The bigger wind stress in E_{35} , E_{31} and E_{34} leads to maximum ice drift speeds (Fig. 8 b) of 0.65, 1.37
581 and 0.70 m/s respectively, and also to larger ocean currents (Fig. 8 c). A maximum ice drift of 0.81
582 m/s, comparable to that from E_{34} , result from E_{11} , where the two coefficients C_{da} and C_{do} differ the
583 least from each other. Smaller values, as expected, result from E_{15} with a maximum of 0.37 m/s and
584 a mean of 0.12 m/s. Sea ice concentration and thickness charts displayed in figures 9 (a, b) reveal
585 that the sea ice distribution in E_{35} , E_{11} and E_{34} show a good comparison, from a qualitative point of
586 view, with MODIS scenes represented in Ciappa et al. (2012). In these experiments the gap between
587 C_{da} and C_{do} is small. In contrast, when C_{do} is much smaller than C_{da} , the ice drift becomes
588 unrealistic and too strong also in regions out of the range of the coastal winds or, in the opposite
589 case, really insignificant along shore. These results supports the importance of the C_{da}/C_{do} ratio
590 considered to be the most basic dynamics parameter determining the mean drift speed (McPhee,
591 1980; Lepparanta, 1981; Stössel, 1992; Geiger et al., 1998; Harder and Fisher, 1999).

592

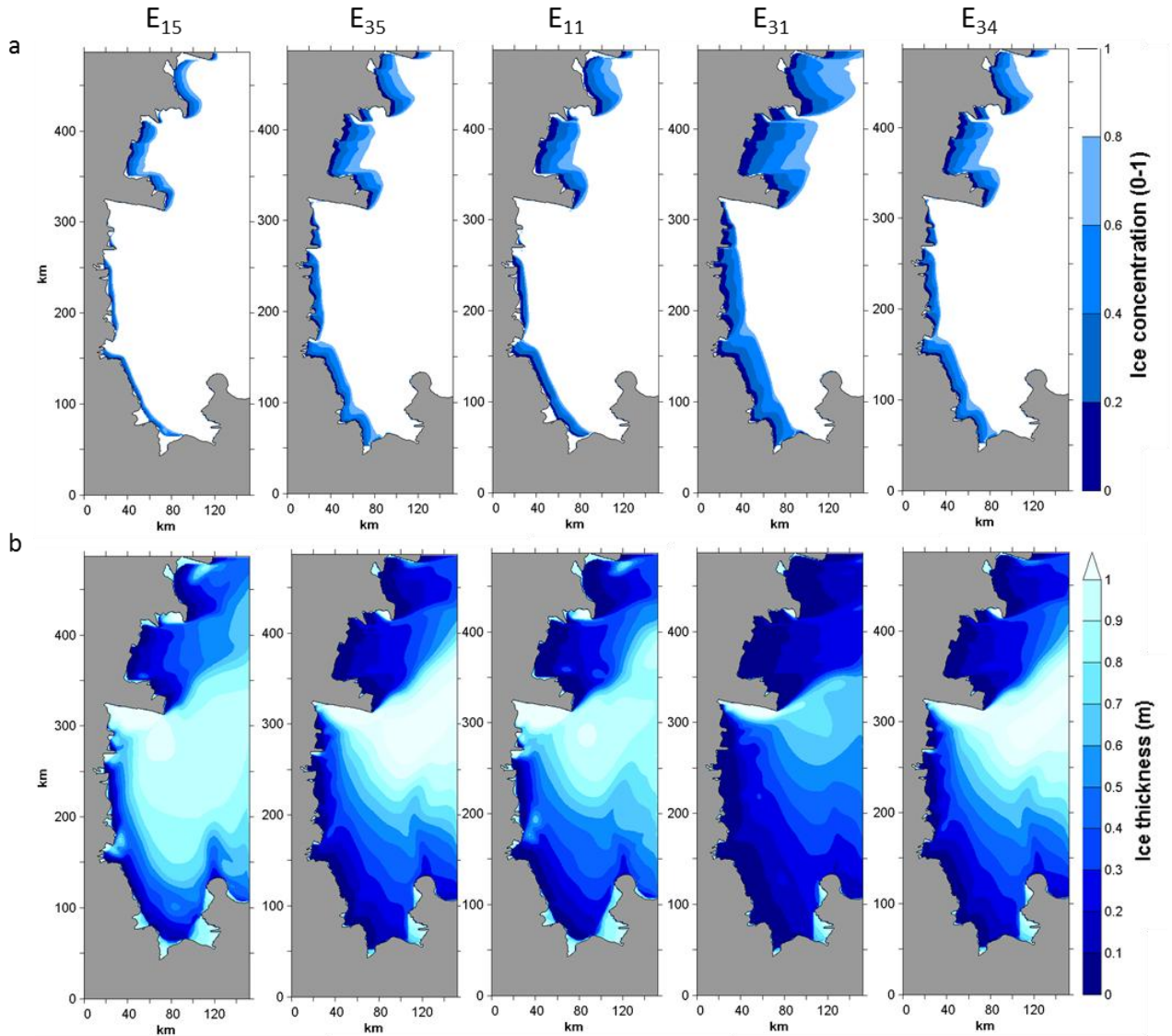


Fig. 9: Modelled sea ice concentration (a) and thickness (b) on 30th July 2005 for E₁₅, E₃₅, E₁₁, E₃₁, E₃₄.

593

594

595 Furthermore, unlike the strength parameter P^* which has a strong impact mainly on thick and more
596 compact areas of the pack ice, the C_{da}/C_{do} ratio influences the ice drift in all regions during all
597 seasons (Kreysner et al., 2000). The dependence of the air-ice drag coefficient on the wind speed
598 has been also investigated by several authors (Large and Pond, 1981; Overland, 1985; Lynch et al.,
599 1997). Accordingly, in the last experiment (E_r) C_{da} was allowed to vary linearly from 1×10^{-3} for
600 wind speeds below 10 m/s, to 3×10^{-3} for wind speeds above 20 m/s. Then, C_{do} is allowed to
601 depend linearly on the C_{da} through a constant factor of 1.3 (McPhee, 1980; Leppäranta, 1981;
602 Stössel, 1992).

603 Figure 10 shows wind and ice velocities with the superimposed wind stress and ice velocity vector
604 fields, ice concentration and thickness maps for E_r on the 30th July 2005 at 24:00. Mean and
605 maximum values of the wind stress are very similar to those resulting from E_{34} . The results of E_r
606 provide the best simulations of the sea ice dynamics of TNB.
607

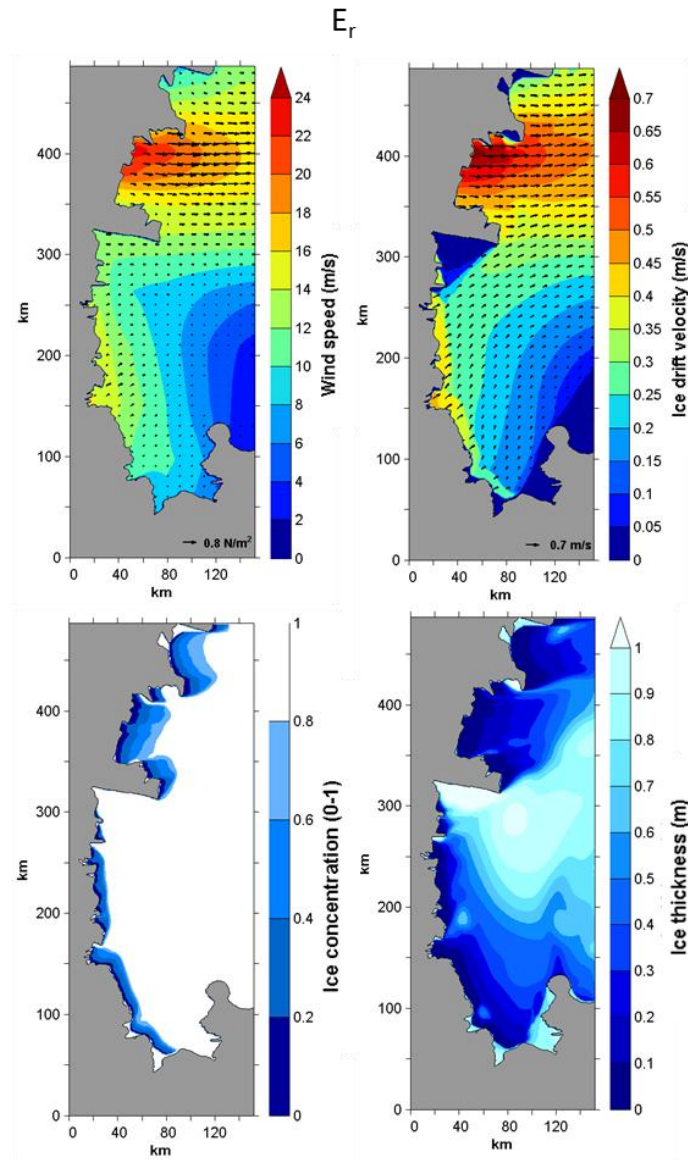


Fig. 10: Wind speeds and modelled sea ice drift velocities with the superimposed wind and ice drift vector field (top) and sea ice concentration and thickness distribution (bottom) on 30th July 2005 for E_r .

610 **4 One year numerical simulation and results**

611 One year simulation of the TNB sea ice evolution has been carried out to investigate the polynya
612 behaviour in response to the local katabatic flows. The main results of the 2005 simulation are
613 discussed. The modelled polynya behaviour follows the characteristic dynamics of sea ice and
614 ocean circulation in TNB. During the summer season, approximately from November to March, the
615 bay is mostly ice free. It starts to be covered by sea ice in late March, when the low atmospheric and
616 oceanic temperatures let the sea surface freeze. The evolution of the polynya is strongly controlled
617 by the action of katabatic winds which allow TNB to be almost never completely ice covered in
618 winter. Katabatic winds are very intense between April and October (Rusciano et al. 2013), and
619 within this period several cycles of opening/closure of the polynya occurred.

620 Model-derived polynya extents in TNB region, defined in the section 3.2, have been computed for
621 2005. The polynya area is usually defined as the sum of the surfaces of open water and thin sea ice
622 and therefore is restricted to the oceanic region within which the ice concentration is smaller than a
623 given threshold (Willmott et al. 2007). This threshold is rather arbitrary, varying commonly from
624 0.5 to 0.7 (Parmiggiani 2006; Kern et al., 2007). An ice concentration threshold of 0.7 has been
625 used here to estimate the TNB polynya extent (Fig. 11).

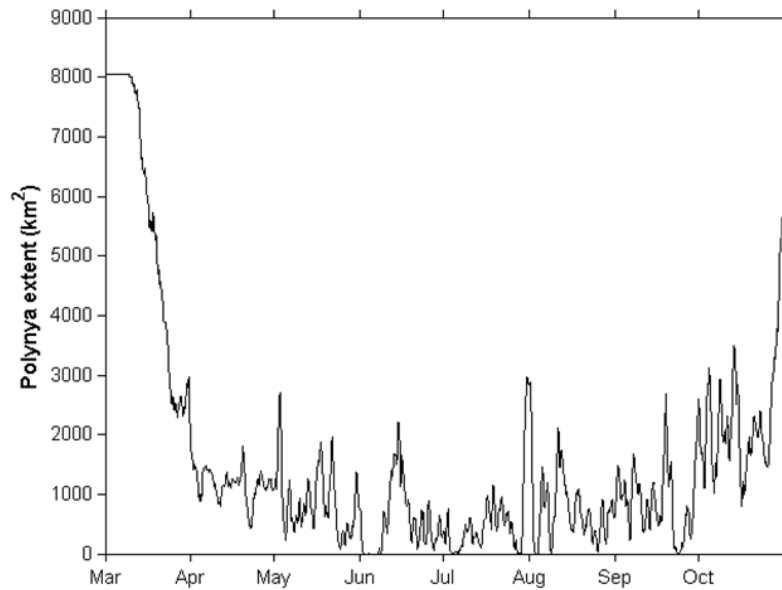


Fig. 11: Model-derived polynya extent in the TNB region from March to October 2005.

626

627 An increase of the polynya size is associated with the occurrence of katabatic events (not shown).

628 The peak extent in midwinter occurred in July with a maximum value of 2962 km², followed by
 629 other two large extents of the polynya in August and September of 2868 km² and 2674 km²
 630 respectively (Table 7).

631 Polynya mean extents vary approximately from just over 500 km² up to almost 900 km², except in
 632 March/April, when sea ice formation processes start, and in October, which represents the end of
 633 the wintertime and the beginning of sea ice melting processes. The computed polynya extents are in
 634 good agreement with the wintertime values estimated by Petrelli et al. (2008) and with those
 635 recently published by Ciappa et al. (2012) who computed a mean annual open water of around 900
 636 km² in the period 2005-2010 and 600 km² in 2006 using MODIS thermal infrared data. In any case,
 637 the computation of the polynya extent is not trivial since it depends on the accuracy and the
 638 limitations of the models and the remote sensing tools, as well as on their capability to resolve in
 639 time and in space the processes involved in the polynya variability. In addition, the local coastal
 640 winds have a strong but not exclusive impact on the polynya size which is caused by the interaction
 641 between katabatic forcing and synoptic weather conditions on longer timescales. The major effect

642 of the katabatic winds on short timescales is the local recirculation of sea ice in TNB and its
643 redistribution within the polynya area (Petrelli et al., 2008). The recirculation forced by these local
644 winds enhances the ice production maintaining high ice production rates in open water and thin ice
645 regions.

Winter months	Maximum Polynya extent (km ²)	Mean Polynya extent (km ²)
March	7946	5574
April	1806	1174
May	2688	871.2
June	2205	557.2
July	2962	532.5
August	2868	766.9
September	2674	875.6
October	5637	2304

650 **Table 7:** Monthly maximum and mean polynya extent of the TNB polynya from March to October 2005.
651

652

653 Sea ice production in the TNB region (Table 8) has been also computed by model sea ice fields
654 outputs. The ice production rate, depends primarily on the presence of open water and on the
655 surface wind speeds, therefore following the same trend as the TNB polynya extent. The spatial
656 maximum sea ice production daily rate over TNB area exhibits a maximum of 0.70 km³/day on 30th
657 July that is equivalent to 48.08 cm/day. These estimates are comparable to those of Petrelli et al.
658 (2008), who simulated the TNB polynya using a coupled atmosphere–sea ice model. She found in
659 her high resolution experiment an ice production maximum daily rate of 26.4 cm/day during winter.
660 Our results are quite consistent, even if slightly smaller, with ice production estimates obtained by
661 Fusco et al. (2002) by applying a one-dimensional flux model to the TNB polynya. She computed
662 for August 1993 and 1994 a maximum value of ice production of 85 cm/day and 72 cm/day
663 respectively. Our daily ice productions result in a cumulative ice production value of 39.29 m over
664 2005 versus her yearly ice production of 81.7 m and 68.8 m for 1993 and 1994. However these
665 larger values in Fusco et al. (2002) were obtained with AWS forcing and the ice production was
666 already significantly reduced when computed using the ECMWF data only. The spatially
667 cumulative daily ice production is also showed in Fig. 12. The highest peaks of ice production occur
668 in May, June and July with maxima of 0.61, 0.54 and 0.70 km³ respectively. The cumulative ice

production, that is the sea ice volume produced in the whole year 2005, is 57.91 km^3 . This value is consistent with the estimation by Tamura et al. (2008) based on satellite data in combination with ERA-40 reanalysis data, which shows for the TNB polynya a mean annual cumulative sea ice production of $59.2 \pm 10 \text{ km}^3$. In particular, the ice volume created in the months of June and July amounts overall to 16.37 km^3 , which is in good agreement with the value of 16.4 km^3 computed by Petrelli et al. (2008) in her winter experiment. The brine rejection, associated with the new ice production, and the HSSW production are also calculated. The brine rejection (kg/day) is parameterized as $P_S = \rho_i P_i (S_1 - S_i) \times 10^{-3}$ (see Markus et al., 1998; Van Woert, 1999a) where P_i is the ice production rate. The HSSW production (m^3/day) is computed following Van Woert (1999a) as $P_{\text{HSSW}} = P_S / \rho_{\text{HSSW}} (S_{\text{HSSW}} - S_{\text{LSSW}}) \times 10^{-3}$ where ρ_{HSSW} is the density of HSSW (1030.45 kg/m^3), S_{HSSW} is the salinity of HSSW (34.8) and S_{LSSW} is the salinity of Low Salinity Shelf Water or Warm Core Water (34.5) (Jacobs et al., 1985).

The salt and HSSW (Fig. 13) production are larger in wintertime, when the ice production is higher. Their cumulative values in the year 2005 within the TNB polynya are $1.7 \times 10^{12} \text{ kg}$ and $0.5 \times 10^{13} \text{ m}^3$ respectively. These values are in good agreement with those of Fusco et al. (2002), Fusco et al. (2009) and Van Woert (1999a). Fusco et al. (2002), for example, estimated a salt production of about $4.6 \times 10^{12} \text{ kg}$ and a HSSW production of $1.5 \times 10^{13} \text{ m}^3$ in the years 1993-94.

Winter months	Maximum daily rates of sea ice production (km^3/day)	Mean daily rates of sea ice production (km^3/day)	Monthly cumulative sea ice (km^3)
March	0.42	0.16	4.99
April	0.40	0.26	7.86
May	0.61	0.30	9.25
June	0.54	0.25	7.52
July	0.70	0.22	6.98
August	0.58	0.30	9.39
September	0.44	0.24	7.34
October	0.39	0.14	4.29

Table 8: Daily sea ice production rates from spatially cumulated ice production in TNB polynya region from March to October 2005.

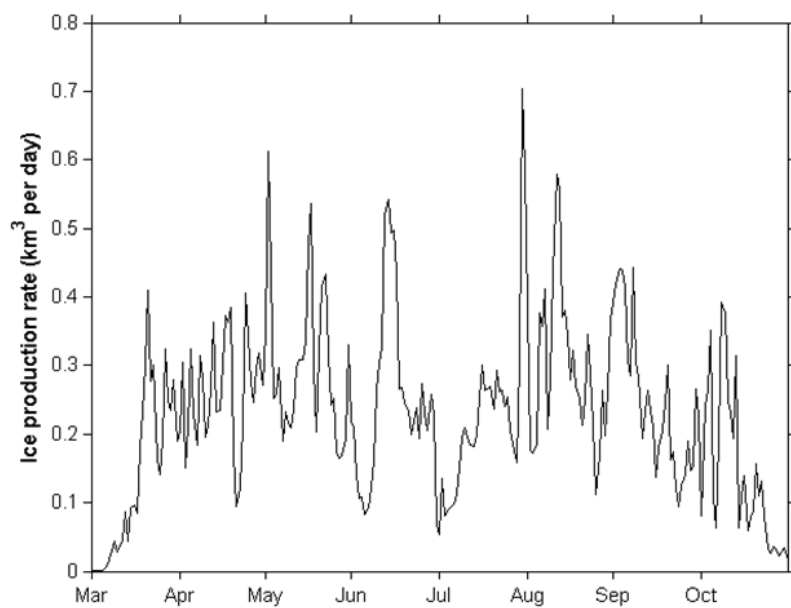


Fig. 12: Spatially cumulated daily rate of sea ice production in the TNB region from March to October 2005.

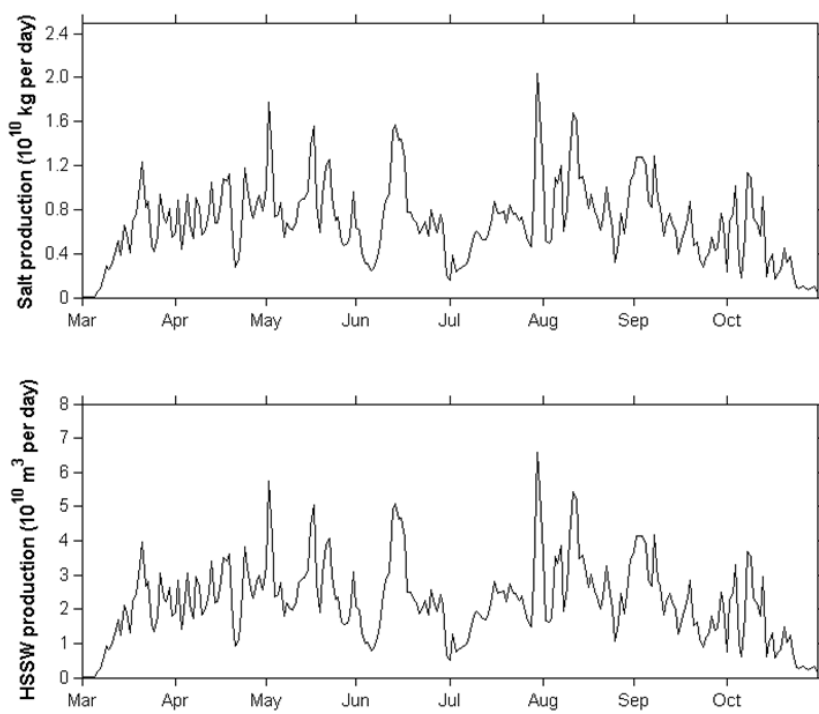


Fig. 13: Daily salt production (top) and HSSW production (bottom) in the TNB region from March to October 2005.

697 **5 Model comparison with MODIS data**

698 In situ measurements are particularly poor in remote or hardly accessible areas during the Antarctic
699 winter, therefore satellite observations represent a useful tool in tuning sea ice-ocean models (Linch
700 et al., 1997). Satellite images in combination with numerical weather prediction model data and in
701 situ data from Automatic Weather Stations provide a good database to study polynya-atmosphere
702 interactions in TNB area (Gallée, 1997; Ciappa et al., 2012).

703 Measurements of ice thickness and total ice volume in Terra Nova Bay do not exist. However, the
704 model can be ground-truthed, at least in part, by comparing the polynya shape and extent to satellite
705 images, which we do in the following. The NASA's MODIS (Moderate Resolution Imaging
706 Spectroradiometer) sensor provides high temporal and spatial resolution measurements of Earth's
707 land, ocean and atmospheric processes in several spectral bands and swath. The MODIS/Aqua
708 Level 1B 1km Calibrated Radiances at 1 km resolution have been used to retrieve the ice surface
709 temperature (IST) in the TNB region and subsequently to derive the polynya extent. Radiance data
710 from MODIS channels 31 and 32 are converted to brightness temperatures (Kelvins) through the
711 inversion of the Planck's law equation (Key et al., 1994). For ice/snow surface temperature (IST)
712 computation the equation based on the technique of Key et al. (1997), originally developed for the
713 Advanced Very High Resolution Radiometer (AVHRR), is used.

714 In order to investigate the dependence of the opening/closing cycles of the polynya on the wind
715 forcing, a few significant periods in the wintertime of 2005 characterized by strong katabatic events
716 have been identified. For each period, sea ice concentration charts from ice fields model outputs
717 have been produced. The polynya edge is identified by the first contour line characterized by an ice
718 concentration threshold of 0.7. These maps have been compared with MODIS IST images obtained
719 following the aforementioned procedure for the same period. Figure 14 and figure 16 show the wind
720 speed from both Rita and Manuela AWSs during two katabatic events observed in May and July

721 (1th - 5th May and 28th - 31th July respectively). The evolution of the polynya extent detected by
722 MODIS can be seen in figures 15 and 17 where the modelled sea ice concentration for the same
723 days is also showed. Sea ice concentration maps at the temporal steps closer to those of satellite
724 scenes have been chosen to match at best model and MODIS products.

725 The model reproduces, reasonably well, sea ice concentration, depth and velocity as seen from the
726 comparison with MODIS images. The drift of sea ice responds to wind forcing which shows a
727 predominant West-West Nord West direction. Stronger winds are responsible for sea ice advection
728 offshore, opening the polynya, and contributing to increasing its extent, while weaker winds just
729 hamper the closure keeping the polynya opened. According to Pease (1987), a seaward wind
730 component exceeding 10m/s is sufficient to maintain a polynya in coastal zones. Our results are in
731 agreement with the suggested threshold.

732

733

734

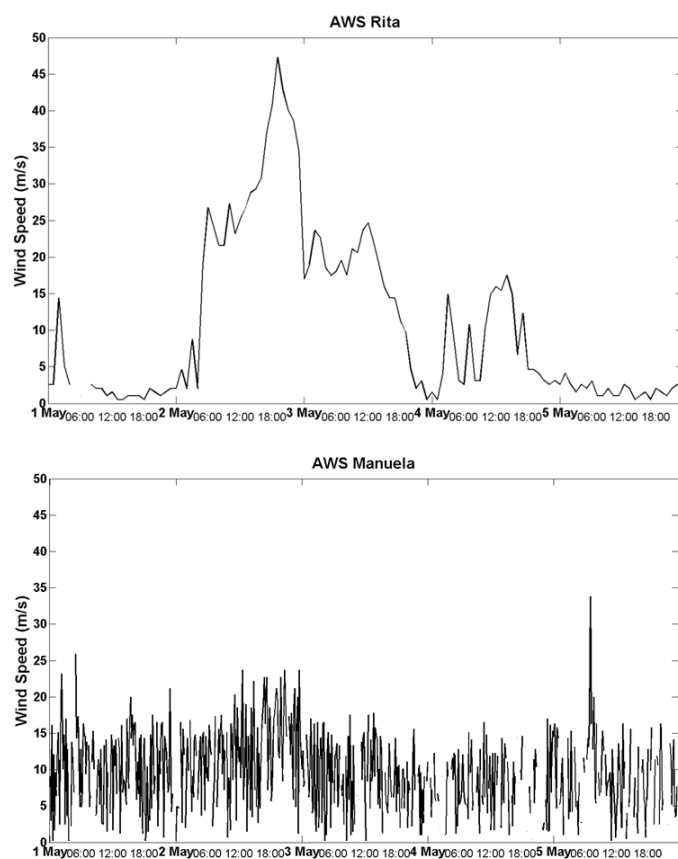


Fig. 14: Wind speed from Rita (top) and Manuela (bottom) AWSs on 1th-5th May 2005.

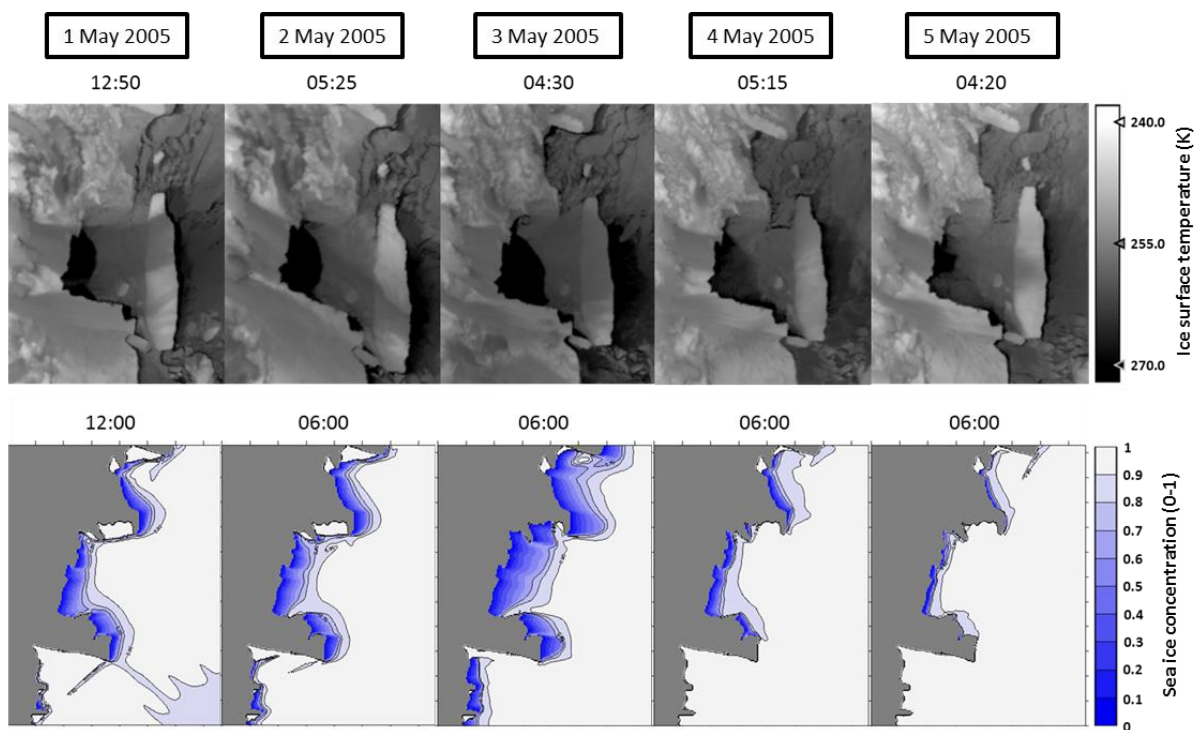


Fig. 15: IST MODIS scenes (top) and the modelled sea ice concentration maps (bottom) displaying the polynya evolution on 1th - 5th May 2005.

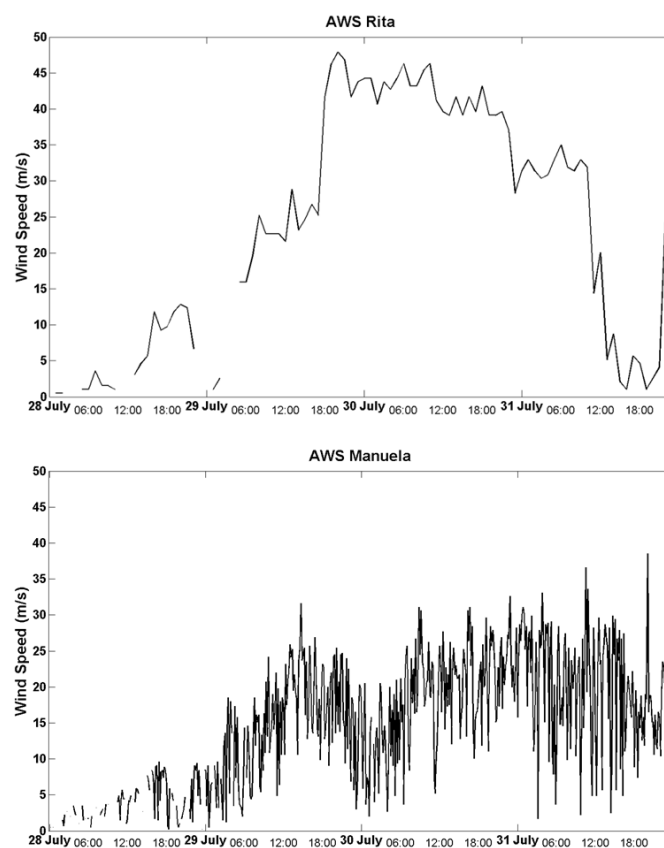


Fig. 16: Wind speed from Rita (top) and Manuela (bottom) AWSs on 28th - 31th July 2005.

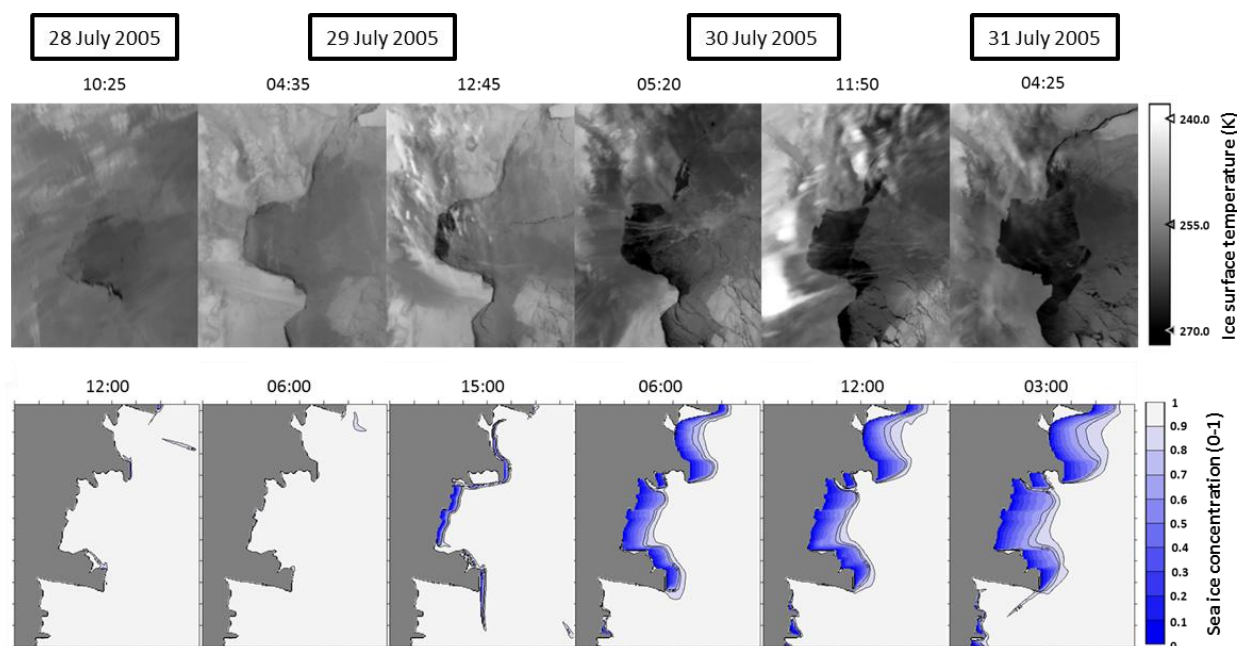


Fig. 17: IST MODIS scenes (top) and the modelled sea ice concentration maps (bottom) displaying the polynya evolution on 28th - 31th July 2005.

741 The small polynya observed at the beginning of the 1st of May (Fig. 15) increases its extent on the
742 2nd day of the month upon an increase of the wind speed measured by the AWS Rita, exhibiting a
743 value well over 20 m/s and reaching a peak of almost 50 m/s. Wind speed from the AWS Manuela
744 with an average value of 20 m/s contributes to enlarge the polynya eastward. The polynya size
745 keeps on increasing at the beginning of 3rd of May until the wind speed drops sharply, below 10 m/s
746 for AWS Rita, and the polynya starts closing on 4th and 5th of May. The small discrepancies
747 between the spatial distribution of sea ice in model simulations and IST MODIS scenes are thought
748 to be partly due to the iceberg B-15A drifting in front of the TNB approximately in April-May
749 2005. The presence of this iceberg blocks the drift of sea ice offshore forcing the ice to accumulate
750 in its proximity. In fact, in IST MODIS scenes the edge of the polynya is located more toward the
751 coast and southward reducing thus the northern portion of the whole polynya extent. The simulation
752 of sea ice distribution in July 2005 (Fig. 17) shows a higher degree of similarity with that observed
753 in satellite images, probably because the advection of sea ice is less affected by the iceberg moving
754 out of the bay. On 28th July the polynya is almost totally closed because the wind speeds are near to
755 zero. After an enhancement of the wind forcing, the polynya starts opening at the beginning of the
756 29th of July and expands rapidly seaward. The largest opening of the polynya occurs on 31th July
757 2005 in response to the stronger wind speeds values recorded previously by AWS stations, near to
758 50 m/s for Rita and 40 m/s for Manuela. Some discrepancies between the simulated polynya and
759 that observed in MODIS scenes may probably due to the gaps (missing data) in the AWSs wind
760 datasets.

761 The TNB polynya extents have been also derived from both MODIS IST scenes and sea ice
762 concentration maps on 28th -31th July. The aforementioned sea ice concentration threshold of 0.7
763 has been used for the modelled ice. A varying threshold for IST proposed by Ishikawa et al. (1996)
764 and Zwally et al. (1983) that discriminates open water and thin ice from thick ice or land fast ice has
765 been employed for satellite maps. Setting sea ice concentration to 0.7, our IST threshold is given by
766 $T_{th} = 0.3T_f + 0.7T_{ice}$ where T_f is the temperature of the open water at the freezing point and T_{ice} is

the temperature of sea ice around the polynya. Both temperature values are extracted from the IST scenes after they have been visually inspected one by one. In particular, T_f is given by the warmest IST found within the polynya and T_{ice} is estimated as the average of the IST values found around the open water.

Polynya extents from the 28th July to the 31th July are showed in Table 9. Polynya extent on the 31th July represents the largest opening of the whole of 2005, as also found in Ciappa et al. (2012). The model-derived polynya extents mostly agree with those computed from MODIS IST images, revealing the same temporal trend in polynya increasing during the observed katabatic event. The polynya extent values are less comparable to the MODIS based extents retrieved by Ciappa et al. (2012) showing a polynya extent of approximately 7615 km² on 31 July at 04:25 versus the corresponding MODIS-derived and model-derived polynya extents of 3393 km² and 2831 km², respectively. That is due to the wider domain considered in his estimates, including all the open water fraction occurred north of TNB (Wood Bay) and south of the Drygalski Ice Tongue.

TNB polynya event in July 2005	Model-derived polynya extent (km²)	MODIS-derived polynya extent (km²)
28 th 12:00	12	40
29 th 06:00	0	25
29 th 15:00	389	391
30 th 06:00	1858	1936
30 th 12:00	2148	2385
31 th 03:00	2831	3393

Table 9: TNB polynya extents from model sea ice concentration outputs and from MODIS IST from 28th to 31th July 2005.

6 Summary and concluding remarks

This work focuses on the investigation of sea ice formation in the TNB polynya in response to wind forcing. Because of the lack of direct observations related to sea ice fields, models provide valuable insight into the mean state of the ice cover (Flato, 2003) together with satellite observations which

indeed fail often in availability and spatial resolution. A coupled sea ice-ocean model that simulates the seasonal cycle of sea ice formation in, and export off, the polynya was presented. The model is applied to the TNB area, including also the nearby regions north and south of the bay in order to characterize at the best seasonal sea ice variability and polynya behaviour. The horizontal resolution is of 1 km, which is sufficient to represent the salient features of the coastline geometry, notably the Drygalski Ice Tongue. The model has been forced by a combination of Era Interim reanalysis by ECMWF and in-situ data from Rita and Manuela AWS, and also by in situ oceanic data.

The modelled sea ice fields have proved to be very sensitive to the atmospheric forcing. The sea ice evolution has been found to be shaped by different parameters involved in the dynamics of sea ice which in turn affects the thermal processes that occur in the ice cover. Several sensitivity experiments have been performed in order to optimize and set up a few main parameterizations and coefficients, thus improving the model outputs. The use of an ice thickness collection depth (H) varying with the wind speed used by Winsor & Björk (2000) seems to be the best choice, amongst the ones considered here, for simulating sea ice fields and thermodynamic heat losses through thin ice inside the polynya. In contrast, the rheology parameter P^* has not been found to affect significantly the drift of sea ice in this region, resulting in almost unchanged outputs of sea ice concentration and thickness distribution irrespective of the value used for P^* . The importance of the air drag coefficient, one of the most important factors in modelling ice motion, has been also stressed. First the responses of the model to constant values of the air-ice (C_{da}) and ice-ocean (C_{do}) drag coefficients and subsequently to the C_{da}/C_{do} ratio have been investigated, the latter being the most basic parameter of sea ice dynamics in determining the mean sea ice drift speed (Geiger et al., 1998; Harder and Fisher, 1999). A C_{da} varying with wind speed has been adopted, while C_{do} is forced to depend linearly on C_{da} through a constant factor. Also a wind enhancement function has been developed in order to try to improve the prediction of sea ice fields. However, its application was unsuccessful, causing too much high values of the wind stress.

817 A simulation of sea ice formation in TNB has been performed for the entire year 2005 to
818 investigate the response of the polynya dynamics to wind forcing. Unsurprisingly, the largest
819 openings of the polynya match the stronger katabatic winds which have been found in wintertime,
820 mainly from April to October. The largest polynya opening occurs in July, with an extent of 2962
821 km², while the polynya extent over the wintertime 2005 ranges between approximately 500 km² and
822 900 km². Sea ice production and the associated brine and HSSW productions have also been
823 computed, exhibiting values cumulated over 2005 of 57.91 km³, 1.7×10^{12} kg and 0.5×10^{13} m³,
824 respectively. These results are in good agreement with those reported by Fusco et al. (2002, 2009)
825 who estimated a salt production of about 4.6×10^{12} kg and a HSSW production of 1.5×10^{13} m³ for
826 the period 1993-1994. In order to support and validate the model outputs, a comparison with sea ice
827 conditions detected by satellite images has been thought essential. Satellite images from then
828 MODIS sensor have been chosen for this purpose since they reach a high spatial resolution of 1 km,
829 the same as that of the model. In order to explore the strong relationship between the wind field and
830 the TNB polynya extent, some wintertime periods including significant katabatic events have been
831 selected. For these periods the MODIS IST scenes have been compared with the modelled sea ice
832 concentration maps. The TNB polynya area seems to be reproduced reasonably well by the model
833 in terms of both shape and distribution of sea ice. However, small differences in sea ice distribution
834 respect to that observed in the MODIS IST scenes are visually detectable in some regions. These
835 differences are most prominent in the areas located along the coast characterized by the variable
836 shelf-ice borders and the presence of land fast ice. In particular, two areas, namely, the region south
837 of Drygalski Ice Tongue and the region north of the TNB (Wood Bay) appear almost recurrently
838 ice free in the modelled sea ice maps.

839 The TNB polynya extent has been also derived from MODIS IST scenes and the corresponding
840 model sea ice maps from the 28th to 31th July 2005. The application of an ice state dependent
841 threshold for IST in MODIS images let us to validate the polynya extent with higher reliability. The
842 model-derived polynya extents are very similar to those computed from MODIS IST images.

843 Finally, despite the discrepancies in both sea ice distribution in some regions and polynya extents,
844 the model performs well in reproducing sea ice evolution. These discrepancies will be investigated
845 more extensively in the future through either an improvement of the model to capture land-fast ice
846 or, more simply the use of a more accurate land mask including fast ice. The remote sensing
847 detection of the polynya area and its extent is obviously affected by fog, clouds or other
848 atmospheric disturbance that often compromise the quality of the used satellite images. At any rate,
849 modelling the opening and closing polynya events is a difficult task especially if the size of polynya
850 is relatively small, as is the case in Terra Nova Bay (Pease, 1987; Lynch et al., 1997; Petrelli et al,
851 2008). Our results have further highlighted the sensitivity of sea ice simulations to wind forcing,
852 which is the major aspect stressed in numerous modelling works on Southern Ocean. Accurate sea
853 ice simulations in terms of sea ice distribution and thickness can be achieved, provided that the
854 model is forced with realistic winds and surface boundary conditions, in particular ocean
855 temperatures, as found by Stössel et al. (2011). High resolution wind forcing is necessary to capture
856 in more detail coastal sea ice processes, such as coastal polynyas, ice drift and ice compression
857 against coastline features.

858

859 **Acknowledgments**

860 The authors are grateful to two reviewers for their constructive comments and suggestions, which
861 have helped to improve the manuscript very significantly. The authors are thankful to the Meteo-
862 Climatological Observatory of the Italian National Program for Research in Antarctica (PNRA) and
863 the Antarctic Meteorological Research Center of the University of Wisconsin-Madison for the
864 Automatic Weather Stations data sets. They are also grateful to the European Centre for Medium-
865 range Weather Forecast for the interim reanalysis and to the MODIS Atmosphere and Archive and
866 Distribution System Nasa Website for free access to MODIS radiance products. This work was

867 performed in the framework of Coastal Ecosystem Functioning in a changing Antarctic ocean
868 project (CEFA) of the PNRA.

869 **References**

- 870
- 871 Biggs N.R.T. and Willmott A.J., 2001: A steady-state coupled ocean-polynya flux model of the North Water, Baffin
872 Bay, *Geophys. Astrophys. Fluid Dyn.*, 95, 1–29.
- 873 Bromwich D. H. 1989: An extraordinary katabatic wind regime at Terra Nova Bay, Antarctica, *Mon Weather Rev.*, 117
874 (3), 688-695.
- 875 Budillon, G., Fusco, G., & Spezie, G., 2000: A study of surface heat fluxes in the Ross Sea (Antarctica). *Antarctic*
876 *Science*, 12(2), 243–254.
- 877 Ciappa A., Pietranera L., and Budillon G., 2012: Observations of the Terra Nova Bay (Antarctica) polynya by MODIS
878 ice surface temperature imagery from 2005 to 2010, *Remote Sens. Environ.*, 119, 158–172.
- 879 Connolley W. M., Gregory J. M., Hunke E. C. and McLaren A. J., 2004: On the consistent scaling of terms in the sea
880 ice dynamics equation. *J. Phys. Oceanogr.*, 1776–1780.
- 881 Cullather R. I., Bromwich D. H. and Grumbine R.W., 1997: Validation of operational numerical analyses in Antarctic
882 latitudes. *J. Geophys. Res.*, 102, 13761-13784.
- 883 Darby M. S., Willmott A. J. and Mysak L. A., 1994: A nonlinear steady-state model of the North Water Polynya, Baffin
884 Bay. *Journal of Physical Oceanography*, 24,1011-1020.
- 885 Darby M. S., Willmott A. J. and Somerville T. A., 1995: On the influence of coastline orientation on the steady state
886 width of a latent heat polynya. *J. Geophys. Res.*, 100, 13,625-13,633.
- 887 Gallée H., 1997: Air-sea interactions over Terra Nova Bay during winter simulation with a coupled atmosphere-polynya
888 model, *J. Geophys. Res.*, 102(D12), 13,835-13,849.
- 889 Geiger C. A., Hibler W. D. and Ackley S. F., 1998: Large-scale sea ice drift and deformation: Comparison between
890 models and observations in the western Weddell Sea during 1992, *J. Geophys. Res.*, 103(C10), 21,893-21,913.
- 891 Fichet T. and Morales Maqueda M.A., 1999: Modelling the influence of snow accumulation and snow-ice formation
892 on the seasonal cycle of the Antarctic sea-ice cover. *Clim. Dyn.*, 15, 251–268.
- 893 Flato G. M., 2003: Sea Ice Modelling. Chapter 9 in *Mass Balance of the Cryosphere: Observations and Modelling of*
894 *Contemporary and Future Changes*, eds. J. Bamber and A. Payne, Cambridge University Press, pg. 367-389.
- 895 Frezzotti, M., and M. C. G. Mabin, 1994: Twentieth century behavior of Drygalski Ice Tongue, Ross Sea, Antarctica,
896 *Ann. Glaciol.*, 20, 397–400.
- 897 Feltham, D.L. 2008. Sea ice rheology. *Annu. Rev. Fluid Mech.*, 40, 91–112.
- 898 Fofonoff, P. and Millard, R.C. Jr, 1983: Algorithms for computation of fundamental properties of seawater, UNESCO
899 Tech. Pap. in Mar. Sci., No. 44, 53 pp
- 900 Fusco G., Flocco D., Budillon G., Spezie G., Zambianchi E., 2002: Dynamics and Variability of Terra Nova Bay
901 Polynya, *Marine Ecology*, 23, 201-209.
- 902 Fusco G., Budillon G., Spezie G., 2009: Surface heat fluxes and thermohaline variability in the Ross Sea and in Terra
903 Nova Bay polynya, *Cont. Shelf Res.* 29, 1887-1895.
- 904 Gent P.R., McWilliams J.C., 1990: Isopycnal mixing in ocean circulation models. *J. Phys. Oceanogr.*, 20, pp. 150–155

905 Harder, M. and Fischer H., 1999: Sea ice dynamics in the Weddell Sea simulated with an optimized model, *J. Geophys.*
 906 *Res.*, 104, 11,151-11,162.
 907 Hibler W. D. III, 1979: A dynamic thermodynamic sea ice model, *J. Phys. Oceanogr.*, 9, 815–846.
 908 Hibler, W. D., III and Walsh J. E., 1982: On modeling the seasonal and interannual fluctuations of Arctic sea ice, *J.*
 909 *Phys. Oceanogr.*, 12, 1514 – 1523.
 910 Holland Paul R., Kwok R., 2012: Wind-driven trends in Antarctic sea-ice drift, *Nature Geoscience* 5, 872-875.
 911 Hunke E. C. and J. K. Dukowicz 1997: An elastic-viscous-plastic model for sea ice dynamics, *J. Phys. Oceanogr.*, 27,
 912 1849-1868.
 913 Ishikawa, T., Ukita, J., Ohshima, K. I., Wakatsuchi, M., Yamanouchi, T., & Ono, N., 1996: Coastal polynyas off East
 914 Queen Maud Land observed from NOAA AVHRR data, *Journal of Oceanography*, 52, 389–398.
 915 Jacobs S. S. and Comiso J. C., 1997: Climate variability in the Amundsen and Bellingshausen Seas. *J. Clim.* 10, 697–
 916 709.
 917 Jacobs S.S., Fairbanks R.G. and Horibe Y., 1985: Origin and evolution of water masses near the Antarctic continental
 918 margins: evidence from H₂ 18O/ H₂ 16O ratios in seawater, *Antarct. Res. Ser.*, 43, 59-85.
 919 Jacobs S. S. and Comiso J. C., 1989: Sea ice and oceanic processes on the Ross Sea continental shelf. *J. Geophys. Res.*,
 920 94, 18195-18211.
 921 Jacobs S. S. and Comiso J. C., 1997: Climate variability in the Amundsen and Bellingshausen Seas. *J. Clim.* 10, 697–
 922 709.
 923 Jacobs S.S., 2004: Bottom water production and its links with the thermohaline circulation, *Antarct. Sci.* 16 (4), 427–
 924 437.
 925 Key J. R., Maslanik J. A., Papakyriakou T., Serreze M. C. and Schweiger A. J., 1994: On the Validation of Satellite-
 926 Derived Sea Ice Surface Temperature, *Arctic*, 47, 3, 280-287.
 927 Key J. R., Collins J. B., Fowler C. and Stone R. S., 1997: High Latitude Surface Temperature Estimates From Thermal
 928 Satellite Data, *Remote Sens. Environ.*, 61, 302-309.
 929 Kern S., Spreen G., Kaleschke L., DE LA Rosa S., and Heygster G., 2007: Polynya Signature Simulation Method
 930 polynya area in comparison to AMSR-E 89 GHz sea-ice concentrations in the Ross Sea and off the Adélie Coast,
 931 Antarctica, for 2002–05: First results, *Ann. Glaciol.*, 46, 409–418.
 932 Kreysher M., Harder M., Lemke P. and Flato G. M., 2000: Results of the Sea-Ice Model Intercomparison Project:
 933 Evaluation of sea ice rheology schemes for use in climate simulations. *J. Geophys. Res.*, 105(C5), 11,299–
 934 11,320.
 935 Kurtz D. D. and Bromwich D. H., 1983: Satellite observed behavior of the Terra Nova Bay polynya. *J. Geophys. Res.*,
 936 88, 9717-9722.
 937 Kurtz D. D. and Bromwich D. H., 1985: A recurring, atmospherically forced polynya in Terra Nova Bay. In
 938 *Oceanology of the Antarctic Continental Shelf*, *Antarct. Res. Ser.*, 43, edited by S. S. Jacobs, 177-201, AGU,
 939 Washington, D.C.
 940 Large W., and Pond S., 1981: Open ocean momentum flux measurements in moderate to strong winds. *J. Phys.*
 941 *Oceanogr.*, 11, 324–336.
 942 Lefebvre W. and Goosse, H., 2005: Influence of the Southern Annular Mode on the sea ice-ocean system: The role of
 943 the thermal and mechanical forcing. *Ocean Sci.* 1, 145–157.
 944 Lemke P., 1987: A Coupled One-Dimensional Sea Ice-Ocean Model, *J. Geophys. Res.*, 92(C12), 13,164–13,172.
 945 Leppäranta, M., 1981: On the structure and mechanics of pack ice in the Bothnian Bay, *Finnish Mar. Res.*, 248, 3–86.

946 Liu J. P., Curry J. A. and Martinson D. G., 2004: Interpretation of recent Antarctic sea ice variability, *Geophys. Res.*
947 *Lett.* 31, L02205.

948 Liu J. P. & Curry J. A., 2010: Accelerated warming of the Southern Ocean and its impacts on the hydrological cycle
949 and sea ice, *Proc. Natl Acad. Sci. USA* 107, 14987–14992.

950 Lynch A. H., Glueck M. F., Chapman W. L., Bailey D. A. and J. E. Walsh, 1997: Satellite observation and climate
951 system model simulation of the St. Lawrence Island Polynya, *Tellus A*, 49, 277–297.

952 Maksym, T., S.E. Stammerjohn, S. Ackley, and R. Massom. 2012. Antarctic sea ice—A polar opposite? *Oceanography*
953 25(3):140–151,

954 Markus, T., Kottmeier C. and Fahrbach E., 1998: Ice formation in coastal polynyas in the Weddell Sea and their impact
955 on oceanic salinity, in *Antarctic Sea Ice: Physical processes, interaction, and variability*, *Antarct. Res. Ser.*, vol.
956 74, edited by M. O. Jeffries, pp. 273 – 292, AGU, Washington, D. C..

957 Martinsen E. A. and Engedahl H., 1987. Implementation and testing of a lateral boundary scheme as an open-boundary
958 condition in a barotropic ocean model. *Coastal Eng.* 11, 603–627.

959 Mathiot, P., Barnier B., Gallée H., Molines J. M., Le Sommer J., Juza M. and Penduff T., (2010): Introducing katabatic
960 winds in global ERA40 fields to simulate their impacts on the Southern Ocean and sea-ice, *Ocean Modell.*, 35,
961 146–160.

962 Maykut, G.A. 1978. Energy exchange over young sea ice in the central Arctic. *J. Geophys. Res.*, 83(C7), 3646–3658.

963 McPhee, M. G., 1980: An analysis of pack ice drift in summer, in *Sea Ice Processes and Models*, edited by R. S.
964 Pritchard, Univ. of Wash. Press, Seattle, 62–75.

965 Monterey G. and Levitus S., 1997: Seasonal Variability of Mixed Layer Depth for the World Ocean. NOAA Atlas
966 NESDIS 14 U.S. Gov Printing Office, , Wash., D.C., 96 pp.

967 Mellor G. L. and Kantha L., 1989: An ice-ocean coupled model, *J. Geophys. Res.*, 94, 10,937–10,954.

968 Morales Maqueda M. Á., Wilmott A. J. and Darby M. S., 1999: A numerical model for intercadal variability of sea ice
969 cover in the Greenland-Iceland-Norwegian Sea, *Climate Dynamics*, 15(2), 89–113.

970 Morales Maqueda M. Á., Willmott A. J., Biggs N. R. T., 2004: Polynya Dynamics: A review of observations and
971 modelling, *Reviews of Geophysics*, 42, RG1004.

972 Mellor G. L. and Kantha L., 1989: An ice-ocean coupled model, *J. Geophys. Res.*, 94, 10,937–10,954.

973 Olason E. O., and Harms I., 2010: Polynyas in a dynamic-thermodynamic sea-ice model, *The Cryosphere*, 4, 147–160.

974 Orsi A. H., Johnson G. C. and Bullister J. L., 1999: Circulation, mixing and production of Antarctic bottom water,
975 *Progress in Oceanography*, 43, Pergamon, 55–109.

976 Ou H. W., 1988: A time-dependent model of a coastal polynya, *J. Phys. Oceanogr.*, 18, 584–590.

977 Overland J. E., 1985: Atmospheric boundary layer structure and drag coefficients over sea ice, *J. Geophys. Res.*, 90,
978 9029–9049.

979 Owens W. B., Lemke P., 1990: Sensitivity studies with a sea ice-mixed layer-pycnocline model in the Weddell Sea. *J.*
980 *Geophys. Res.*, 95, C6, 9527–9538.

981 Pacanowski R. and Philander S.G.H., 1981: Parameterization of vertical mixing in numerical models of tropical oceans,
982 *J. Geophys. Res.* 11, 1443–1451.

983 Parkinson C. L. and Cavalieri D. J., 2012: Antarctic sea ice variability and trends, 1979–2010, *The Cryosphere*, 6, 871–
984 880.

985 Parmiggiani, F. 2006: Fluctuations of Terra Nova Bay polynya as observed by active (ASAR) and passive (AMSR-E)
986 microwave radiometers, *Int. J. Remote Sensing*, 27(12), 2459–2467.

987 Pease C. H., 1987: The size of wind-driven coastal polynyas, *J. Geophys. Res.*, 92, 7049–7059.

988 Petrelli P., Bindoff N. L. and Bergamasco A., 2008: The sea ice dynamics of Terra Nova Bay and Ross Ice Shelf
989 Polynyas during a spring and winter simulation, *J. Geophys. Res.*, 113.

990 Rothrock D. A., 1979: Modeling sea-ice features and processes, *Journal of Glaciology*, 24, 90.

991 Rusciano E., Budillon G., Fusco G., and Spezie G., 2013: Evidence of atmosphere-sea ice-ocean coupling in the Terra
992 Nova Bay polynya (Ross Sea-Antarctica), *Continental Shelf Research* 61-62, 112-124.

993 Russell J.L., Stouffer R.J., and Dixon K.W., 2006: Intercomparison of the Southern Ocean circulations in IPCC coupled
994 model control simulations, *J. Clim.* 19:4,560–4,575.

995 Semtner A. J., 1976: A model for the thermodynamic growth of sea ice in numerical investigations of climate, *J. Phys.*
996 *Oceanogr.*, 6, 27–37.

997 Steele, M., J. Zhang, D. Rothrock and H. Stern. 1997. The force balance of sea ice in a numerical model of the Arctic
998 Ocean. *J. Geophys. Res.*, 102(C9), 21,061–21,079.

999 Stössel A., Lemke P. and Owens W.B., 1990: Coupled sea ice-mixed layer simulations for the Southern Ocean, *J.*
1000 *Geophys. Res.*, 95, 9539-9555.

1001 Stössel A., 1992: Sensitivity of the Southern Ocean sea-ice simulations to different atmospheric forcing algorithms,
1002 *Tellus A*, 395-413.

1003 Stössel A., Zhang Z., and Vihma T., 2011: The effect of alternative real-time wind forcing on Southern Ocean sea-ice
1004 simulations, *J. Geophys. Res.*, 116, C11021.

1005 Tamura T., Ohshima Kay I. and Nihashi S., 2008: Mapping of sea ice production for Antarctic coastal polynyas, *J.*
1006 *Geophys. Lett.*, 35.

1007 Tear S., Willmott A.J., Biggs N.R.T., Morales Maqueda M.A., 2003: One-dimensional models for the closure of a
1008 coastal latent heat polynya, *J. Phys. Oceanogr.* 33, 329–342.

1009 Trumbore S.E., Jacobs S. S. and Smethie JR W. M., 1991: Chlorofluorocarbon evidence for rapid ventilation of the Ross
1010 Sea. *Deep-Sea Research*, 38, 845-870.

1011 Turner J., Comiso J. C., Marshall G. J., Lachlan-Cope T. A., Bracegirdle T., Maksym T., Meredith M. P., Wang Z., and
1012 Orr A., 2009: Non-annular atmospheric circulation change induced by stratospheric ozone depletion and its role
1013 in the recent increase of Antarctic sea ice extent, *Geophys. Res. Lett.*, 36, L08502.

1014 Van Woert M. L., 1999a: The wintertime expansion and contraction of the Terra Nova Bay polynya. In *Oceanography*
1015 *of the Ross Sea: Antarctica*, edited by G. Spezie and G. M. R. Manzella, pp. 145-164, Springer-Verlag, New
1016 York.

1017 Van Woert M. L., 1999b: Wintertime dynamics of the Terra Nova Bay polynya. *J. Geophys. Res.*, 104, 7753-7769.

1018 Willmott A. J., Holland D. M. and Morales Maqueda, M. A., 2007: Polynya modelling. In: Smith, Walker, O.; Barber,
1019 David, G., (eds.) *Polynyas: windows to the world*. Amsterdam, Elsevier, 87-125. (Elsevier Oceanography Series,
1020 74).

1021 Winsor P. and Björk G., 2000: Polynya activity in the Arctic Ocean from 1958 to 1997, *J. Geophys. Res.*, Oceans 105,
1022 8789-8803.

1023 Winsor P. and Björk G., 2000: Polynya activity in the Arctic Ocean from 1958 to 1997, *J. Geophys. Res.*, Oceans 105,
1024 8789-8803.

1025 Zhang J, 2007: Increasing Antarctic Sea Ice under Warming Atmospheric and Oceanic Conditions, *J. Climate*, 20,
1026 2515–2529.

1027 Zwally H. J., Comiso J. C., Parkinson C. L., Campbell W. J., Carsey F. D., and Gloersen P., 1983: Antarctic Sea Ice,
1028 1973–1976: Satellite Passive-Microwave Observations, Washington, DC, National Aeronautics and Space
1029 Administration, 206 pp.
1030

1031 **Figure and table captions**

1032 **Fig. 1:** Overview map of TNB (Western Ross Sea) showing the major geographical features of this
1033 region and its surroundings (Kurtz and Bromwich, 1983).

1034 **Fig. 2:** Schematic view of the main variables of the coupled sea ice – ocean model. The radiative
1035 and turbulent heat fluxes are separately calculated over the ice free (leads) and ice covered areas.

1036 **Fig. 3:** The model domain showing the Drygalski Ice Tongue (DIT) and the two preferential paths
1037 of the katabatic flows, the Priestley and the Reeves Glaciers. The Italian base, Mario Zucchelli
1038 Station (MZS), and the location of the automatic weather stations, Rita (AWS-R: 74.72°S,
1039 164.03°E) and Manuela (AWS-M: 74.95°S, 163.69°E) are also indicated.

1040 **Fig. 4:** Diagram flow of the coupled sea ice - ocean model.

1041 **Fig. 5:** Maps of wind speed (a), modelled ice drift velocity (b) and modelled ocean current (c)
1042 overlaid by the corresponding wind speed vectors, ice drift velocity vectors and ocean current
1043 vectors on 8th July 2000 for CASE 1 to CASE 4.

1044 **Fig. 6:** Maps of modelled sea ice concentration (a) and thickness (b) on 8th July 2000 for CASE 5,
1045 CASE 6, CASE 7, CASE 8 and CASE 9.

1046 **Fig. 7:** Daily ice production (left) on July 2000 for CASE 5 to CASE 9 within a smaller area of the
1047 domain, defined as TNB region (right), extending approximately from 310 km to 425 km in Y and
1048 bordered by X = 120 km.

1049 **Fig. 8:** Wind speeds (a), sea ice drift velocities (b) and ocean currents (c) with the superimposed
1050 wind stress, ice drift and ocean current vectors, respectively on 30th July 2005 for E₁₅, E₃₅, E₁₁, E₃₁,
1051 E₃₄.

1052 **Fig. 9:** Modelled sea ice concentration (a) and thickness (b) on 30th July 2005 for E₁₅, E₃₅, E₁₁, E₃₁,
1053 E₃₄.

1054 **Fig. 10:** Wind speeds and modelled sea ice drift velocities with the superimposed wind and ice drift
1055 vector field (top) and sea ice concentration and thickness distribution (bottom) on 30th July 2005 for
1056 E_r.

1057 **Fig. 11:** Model-derived polynya extent in the TNB region from March to October 2005.

1058 **Fig. 12:** Spatially cumulated daily rate of sea ice production in the TNB region from March to
1059 October 2005.

1060 **Fig. 13:** Daily salt production (top) and HSSW production (bottom) in the TNB region from March
1061 to October 2005.

1062 **Fig. 14:** Wind speed from Rita (top) and Manuela (bottom) AWSs on 1th - 5th May 2005.

1063 **Fig. 15:** IST MODIS scenes (top) and the modelled sea ice concentration maps (bottom) displaying
1064 the polynya evolution on 1th - 5th May 2005.

1065 **Fig. 16:** Wind speed from Rita (top) and Manuela (bottom) AWSs on 28th - 31th July 2005.

1066 **Fig. 17:** IST MODIS scenes (top) and the modelled sea ice concentration maps (bottom) displaying
1067 the polynya evolution on 28th - 31th July 2005.

1068

1069 **Table 1:** Input parameters of the model. The “x” stands for a varying value assigned to that
1070 parameter in the sensitivity experiments.

1071 **Table 2:** Physical parameters of atmosphere, sea ice and ocean.

1072 **Table 3:** Sensitivity tests of sea ice evolution with respect to P^* and R factor.

1073 **Table 4:** Sensitivity tests of sea ice evolution with respect to H and R factor.

1074 **Table 5:** Sea ice production in July 2000 for the experiments CASE 5 to CASE 9.

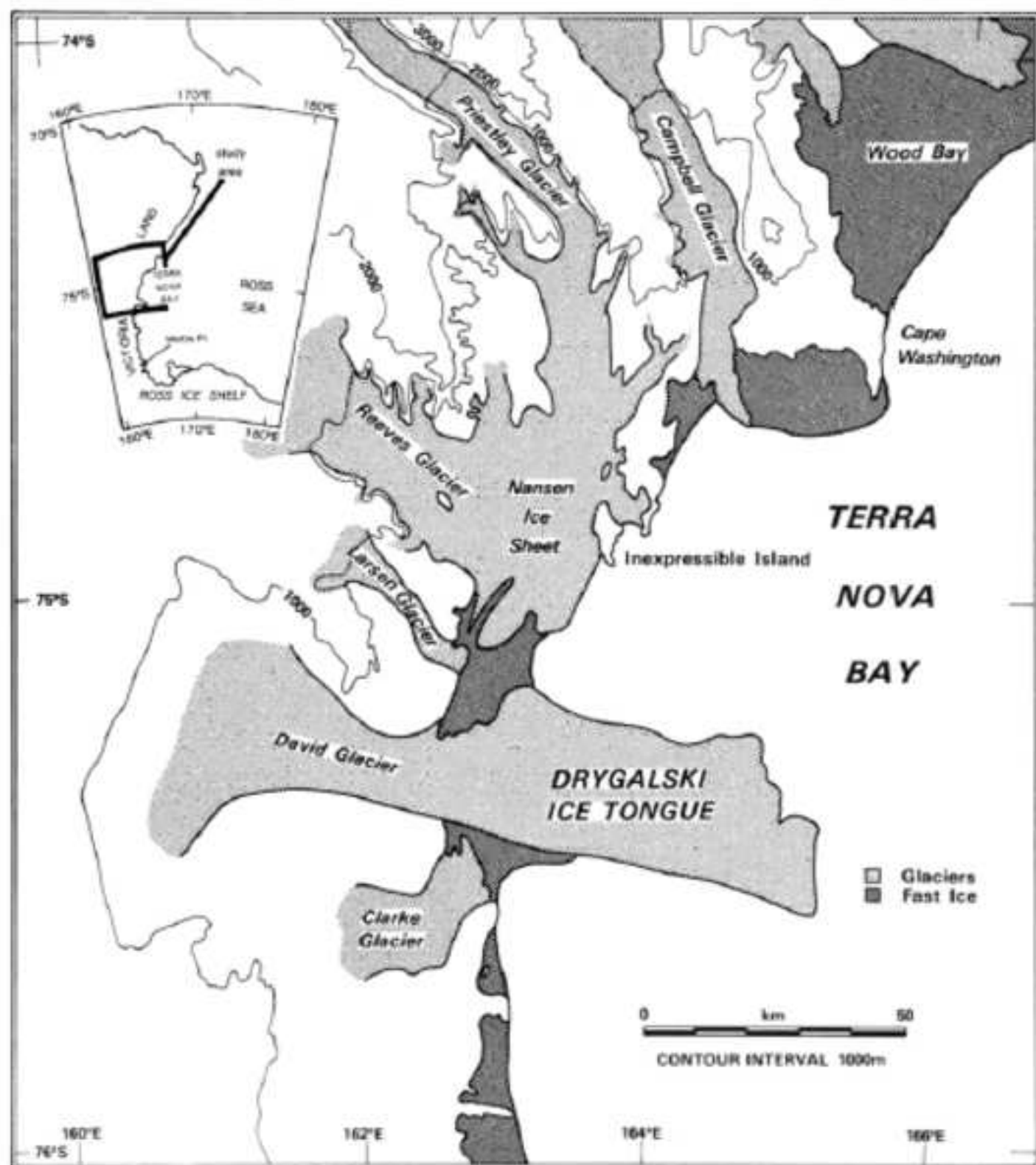
1075 **Table 6:** Sensitivity tests with respect to the air-ice and ice-ocean drag coefficients. The double
1076 sub-index identifies the wind and ocean drag coefficients used in each experiment.

1077 **Table 7:** Monthly maximum and mean polynya extent of the TNB polynya from March to October
1078 2005.

1079 **Table 8:** Daily sea ice production rates from spatially cumulated ice production in TNB polynya
1080 region from March to October 2005.

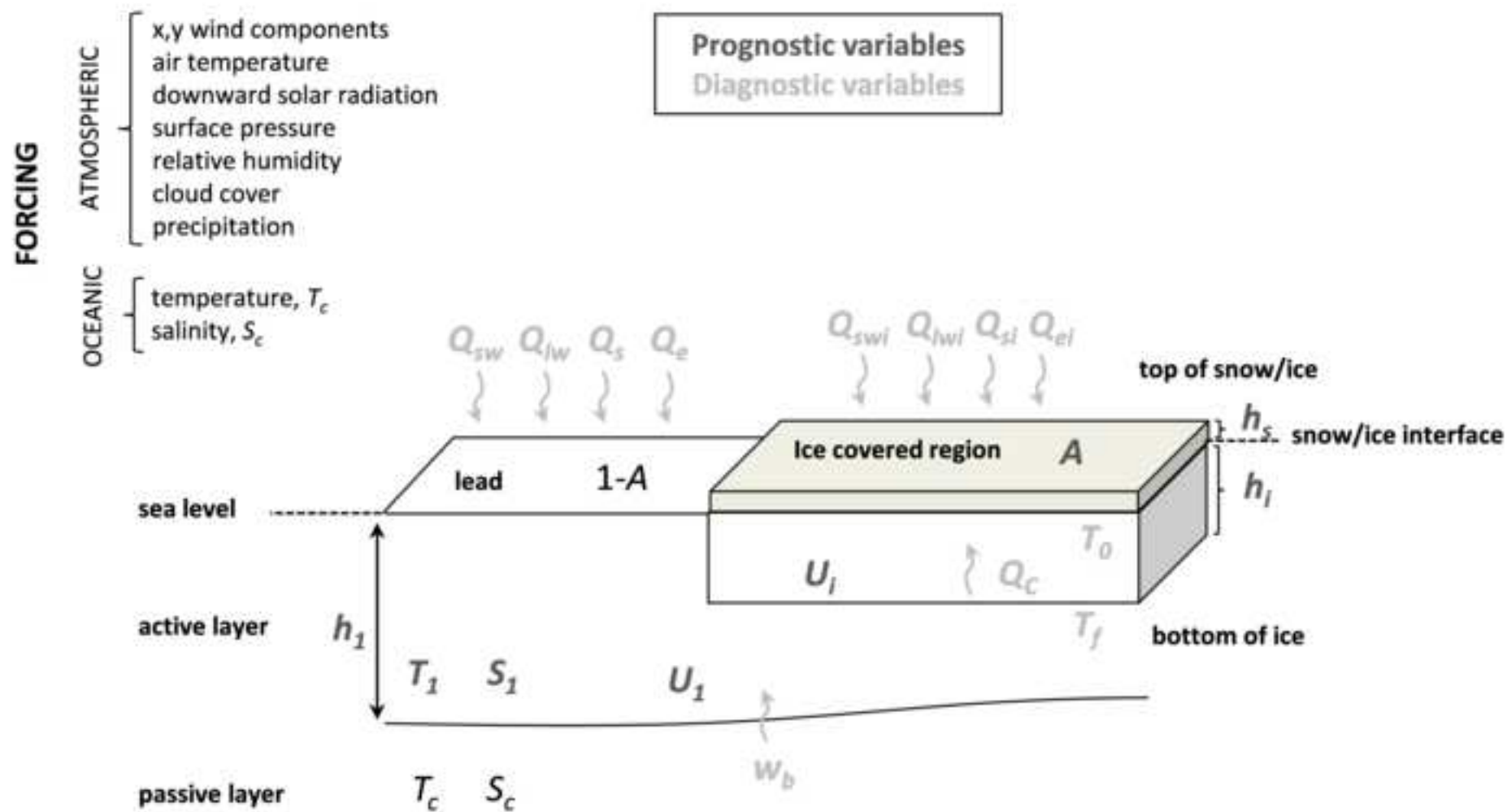
1081 **Table 9:** TNB polynya extents from model sea ice concentration outputs and from MODIS IST
1082 from 28th to 31th July 2005.

Figure(s)
[Click here to download high resolution image](#)

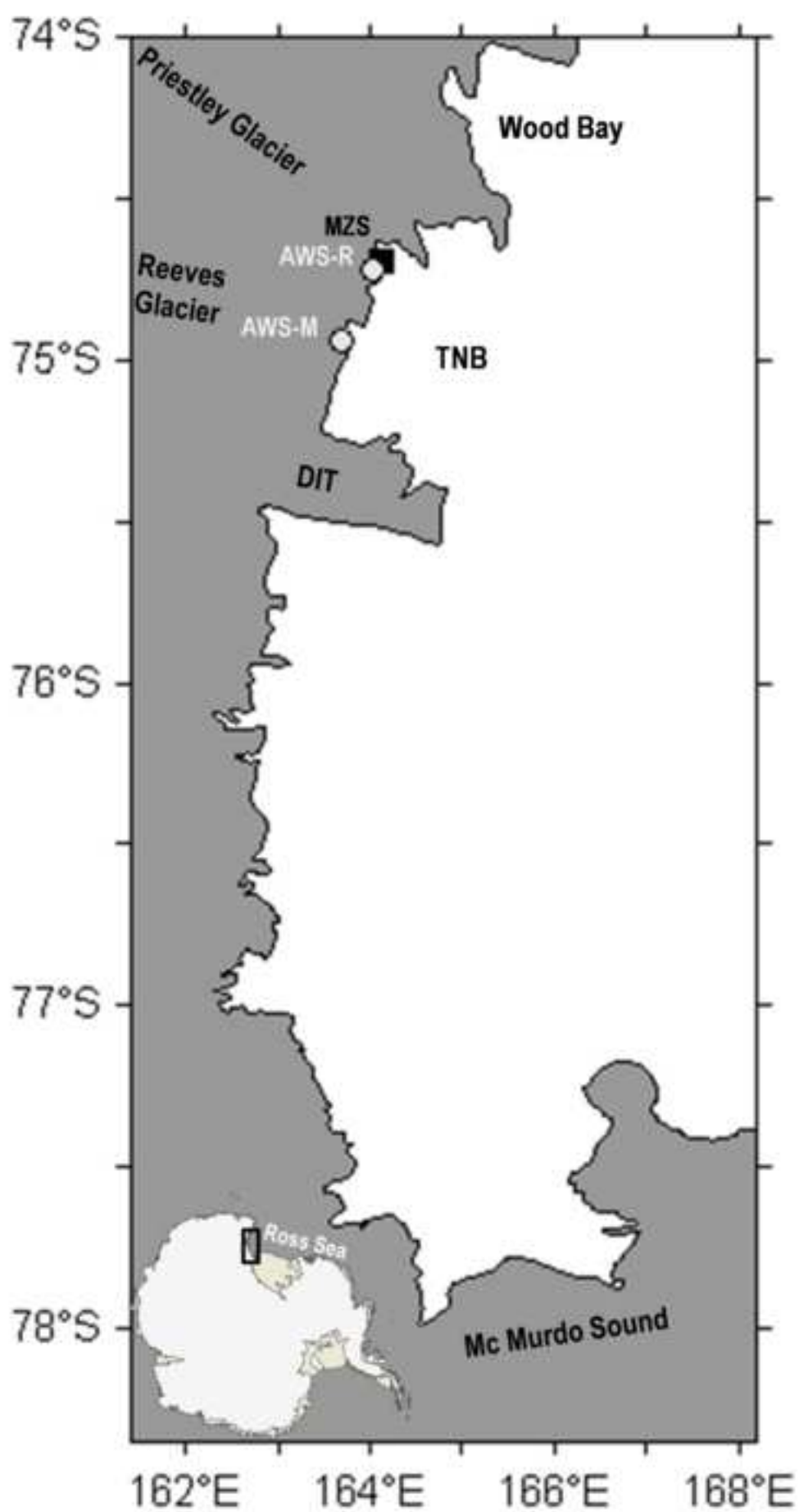


Figure(s)

[Click here to download high resolution image](#)

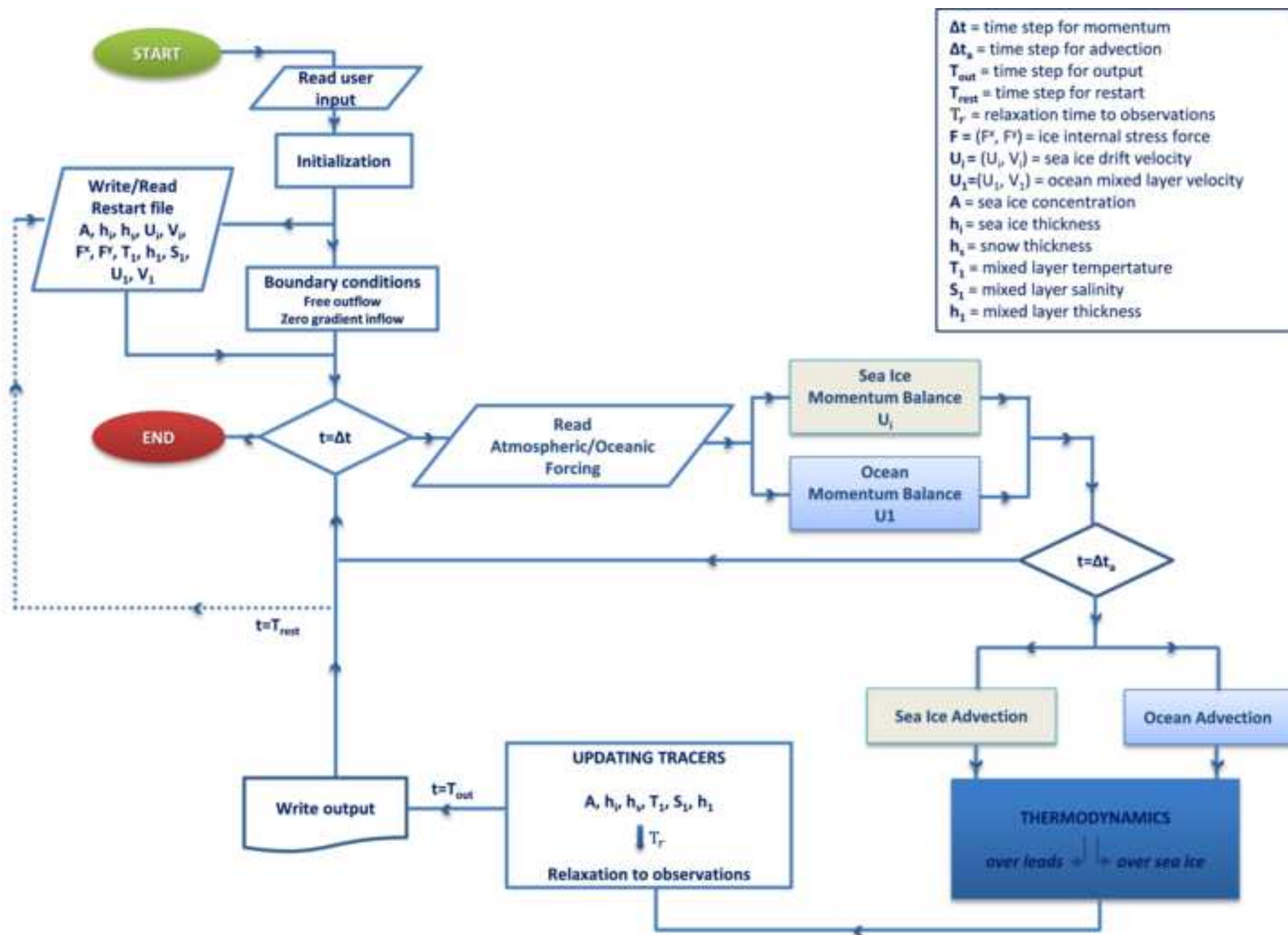


Figure(s)
[Click here to download high resolution image](#)

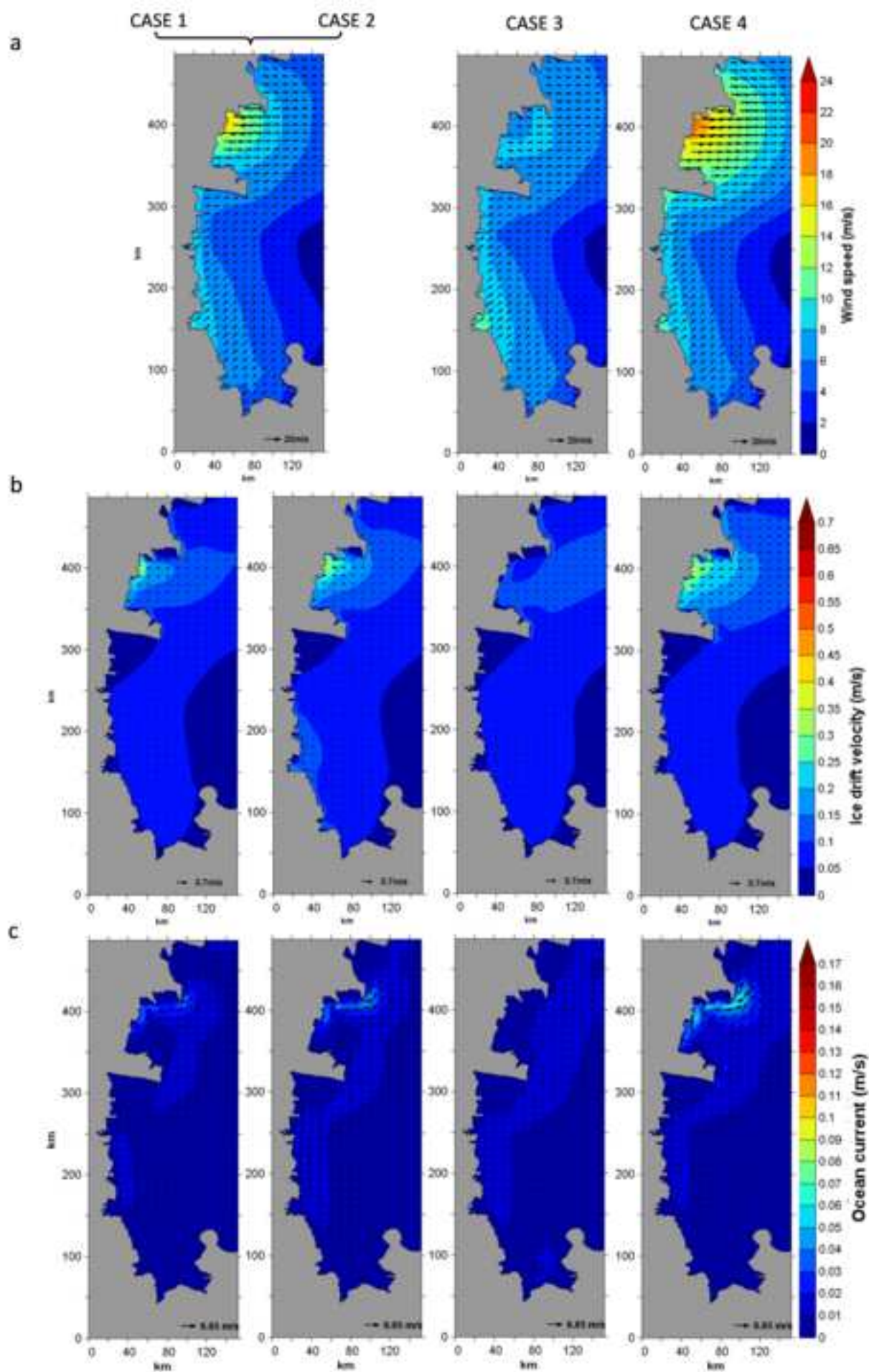


Figure(s)

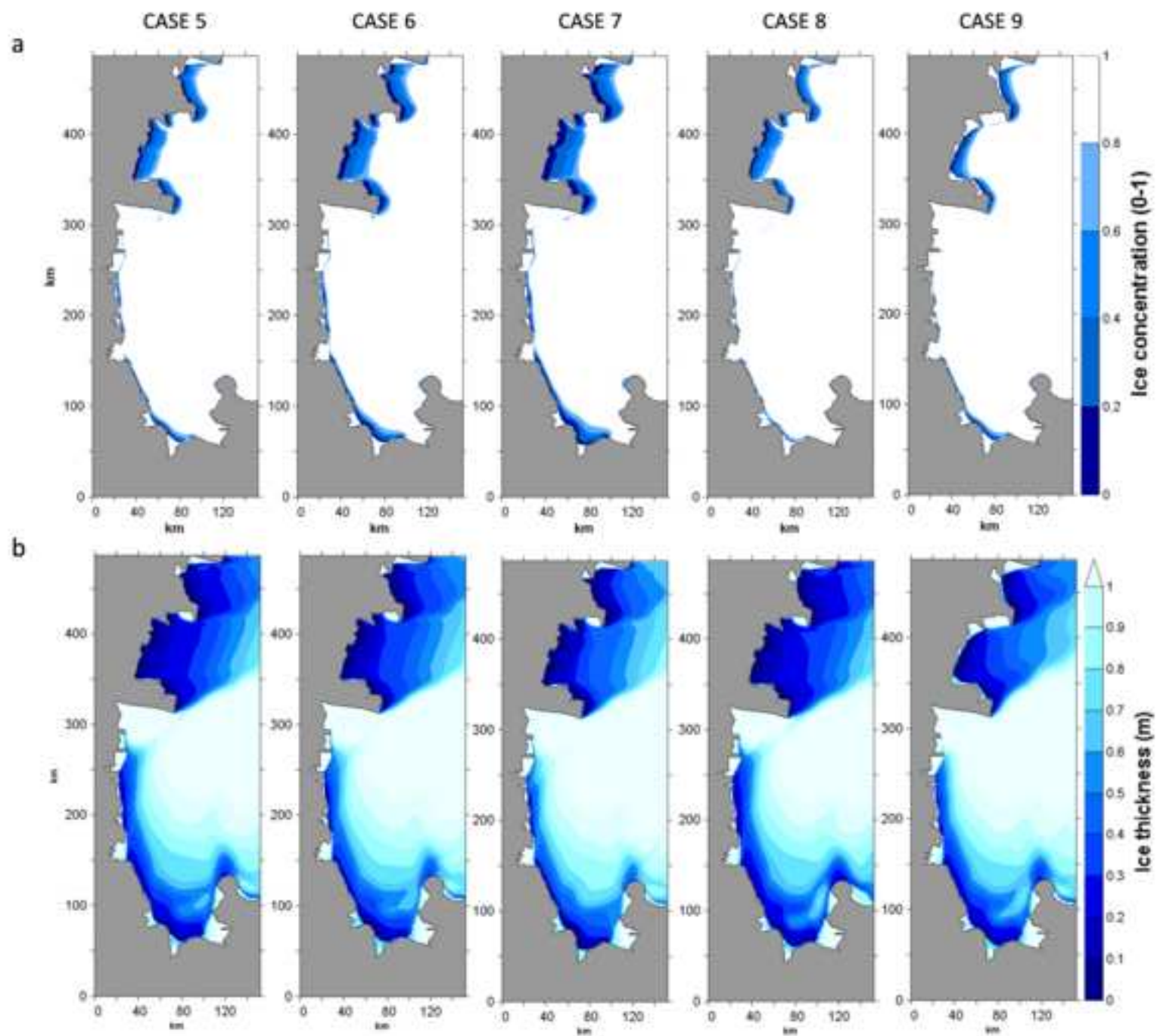
[Click here to download high resolution image](#)



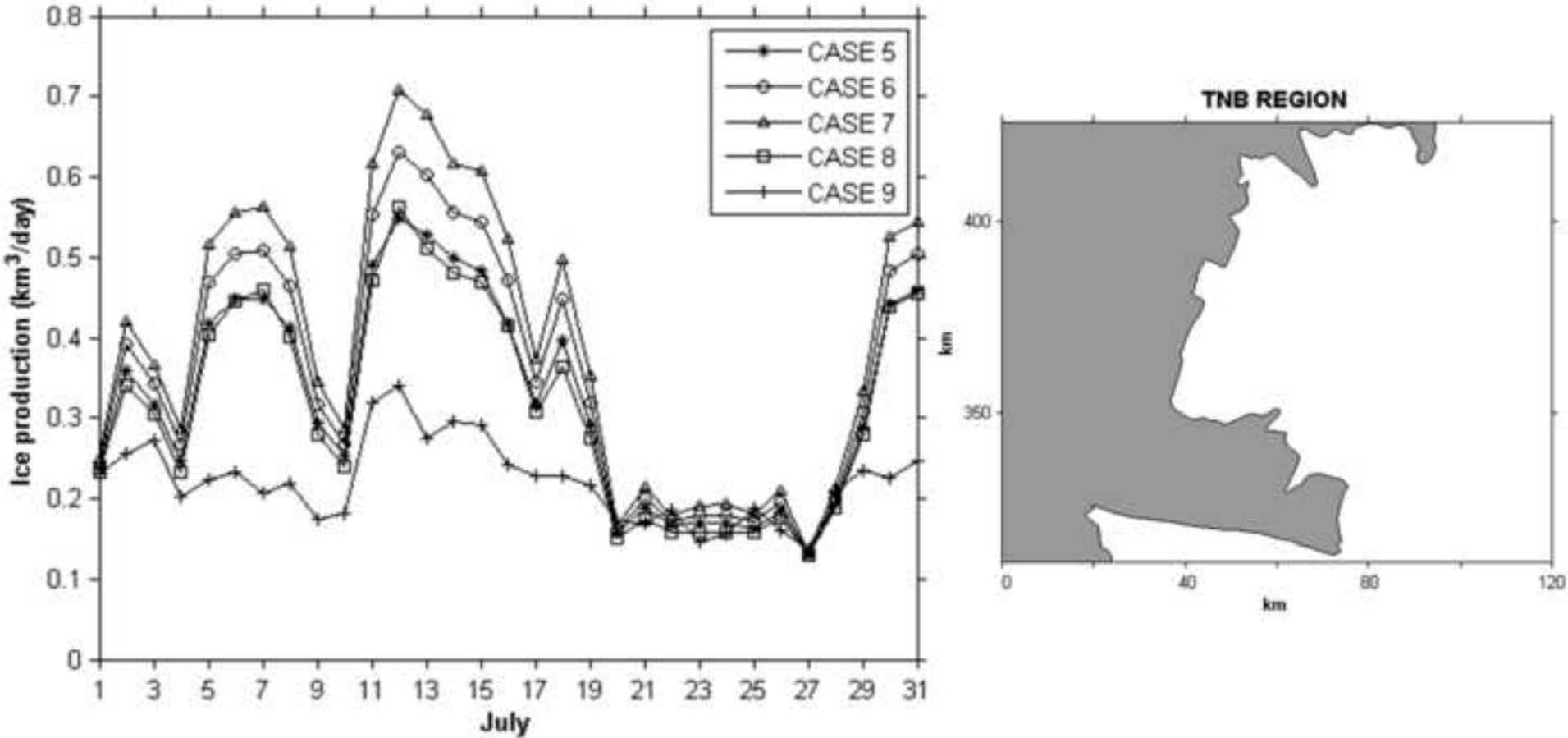
Figure(s)
[Click here to download high resolution image](#)



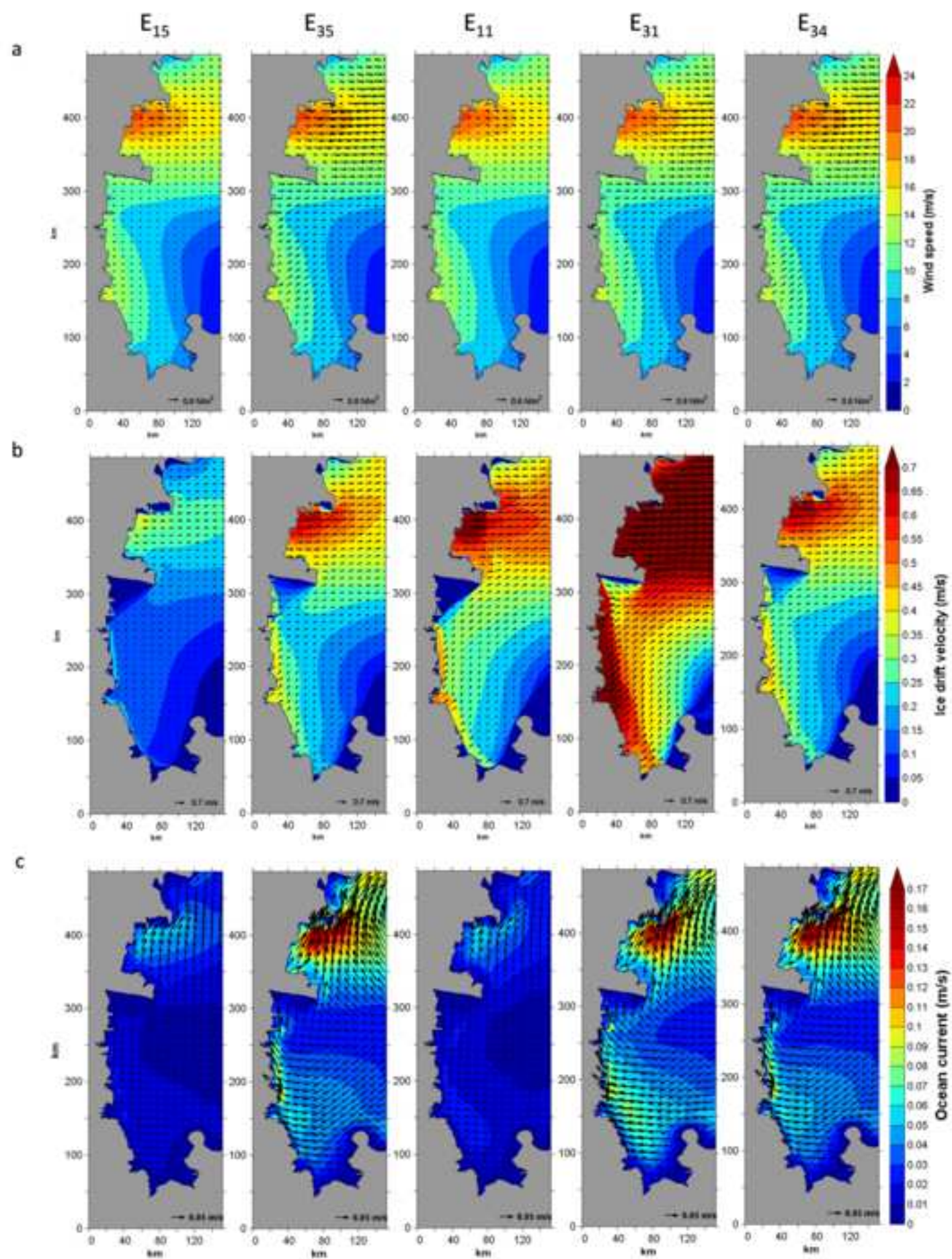
Figure(s)
[Click here to download high resolution image](#)



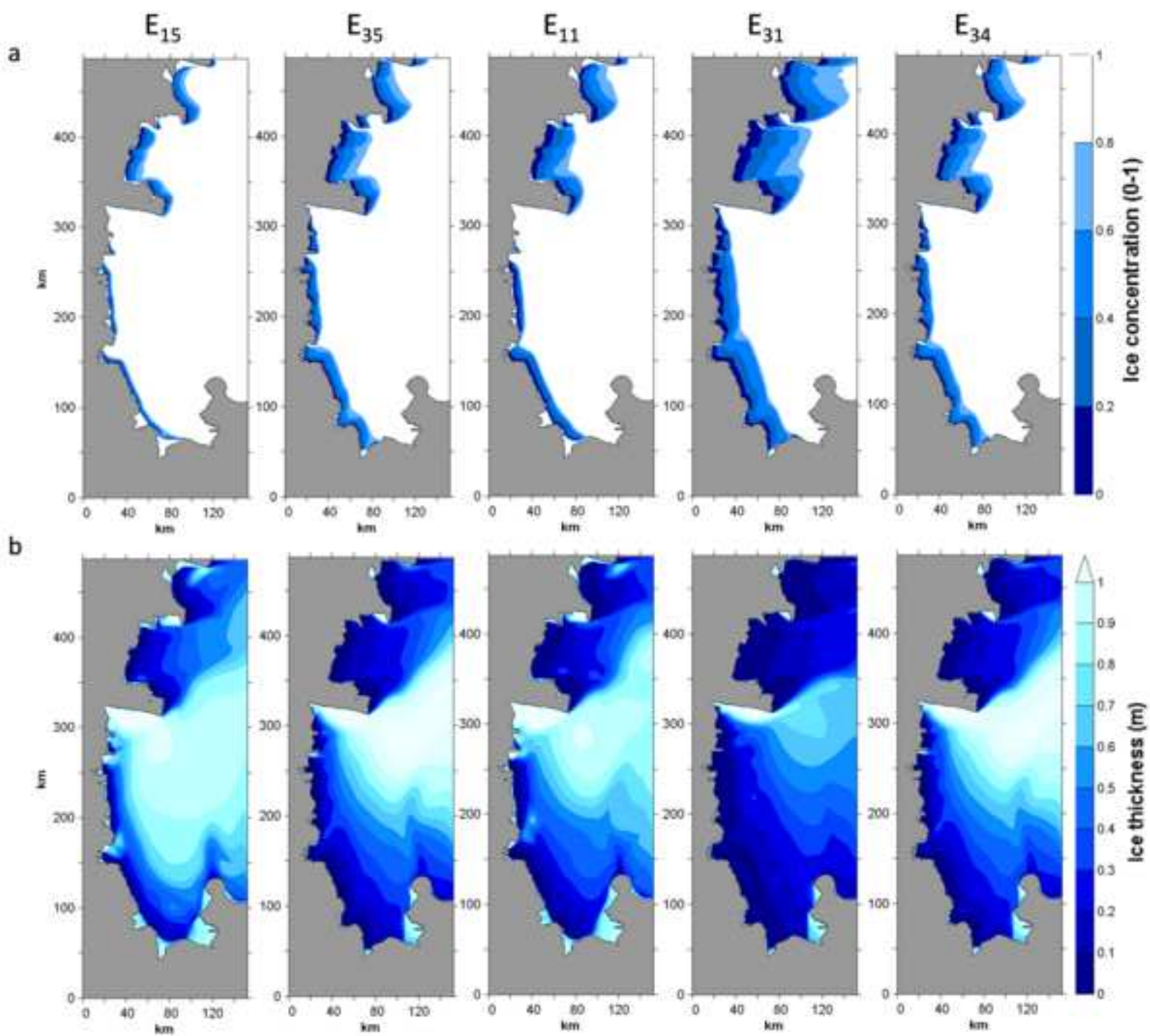
Figure(s)
[Click here to download high resolution image](#)

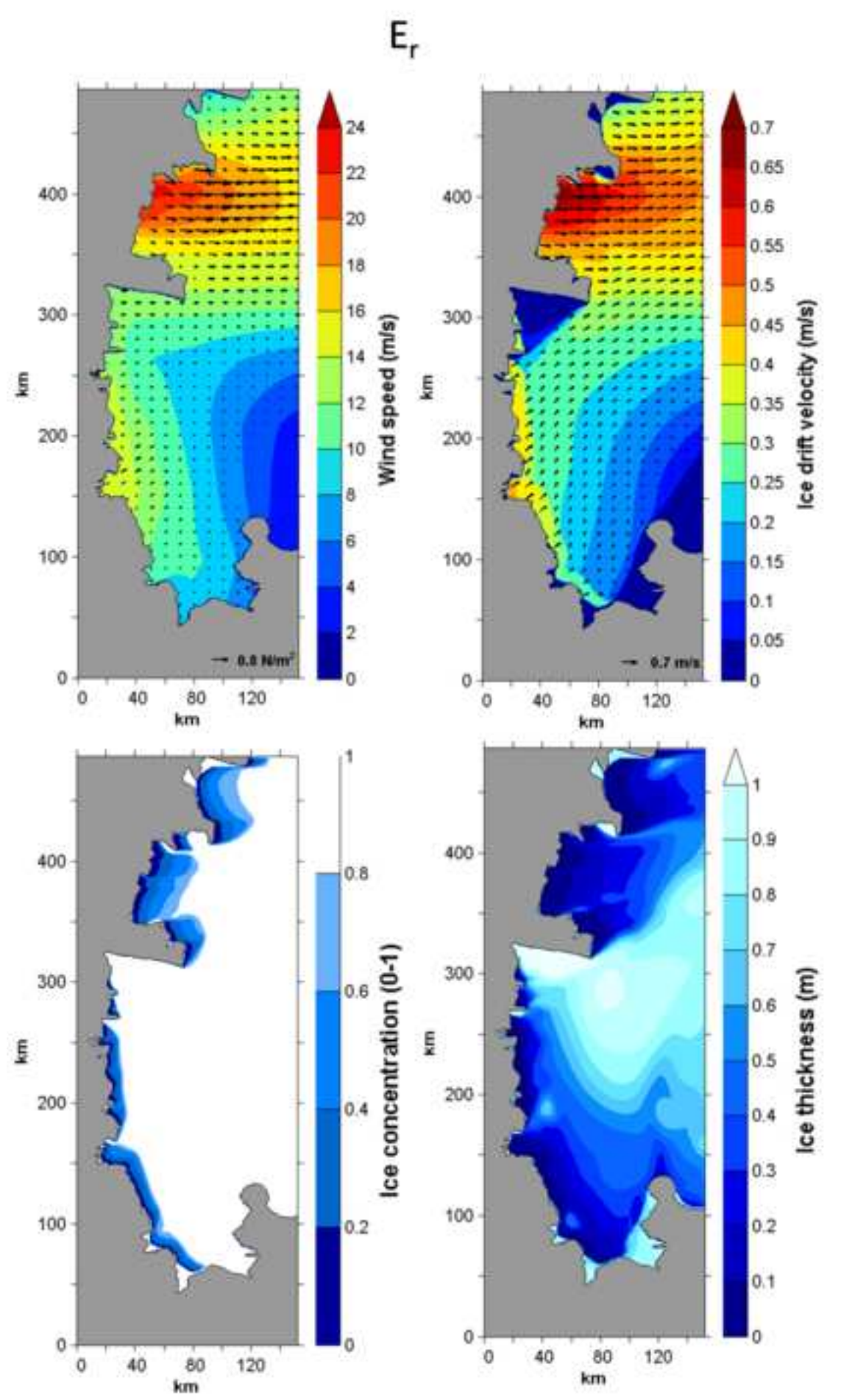


Figure(s)
[Click here to download high resolution image](#)

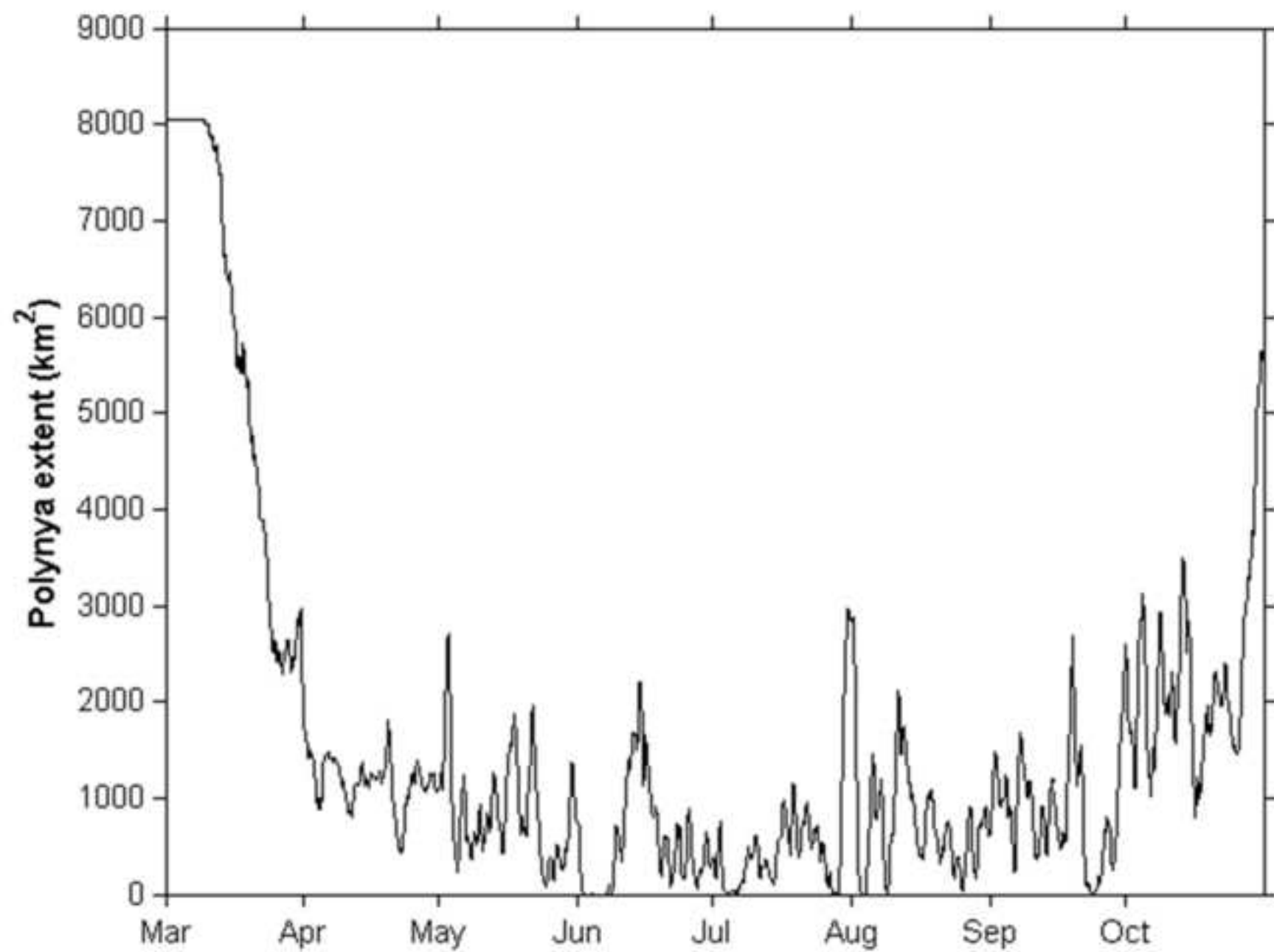


Figure(s)
[Click here to download high resolution image](#)



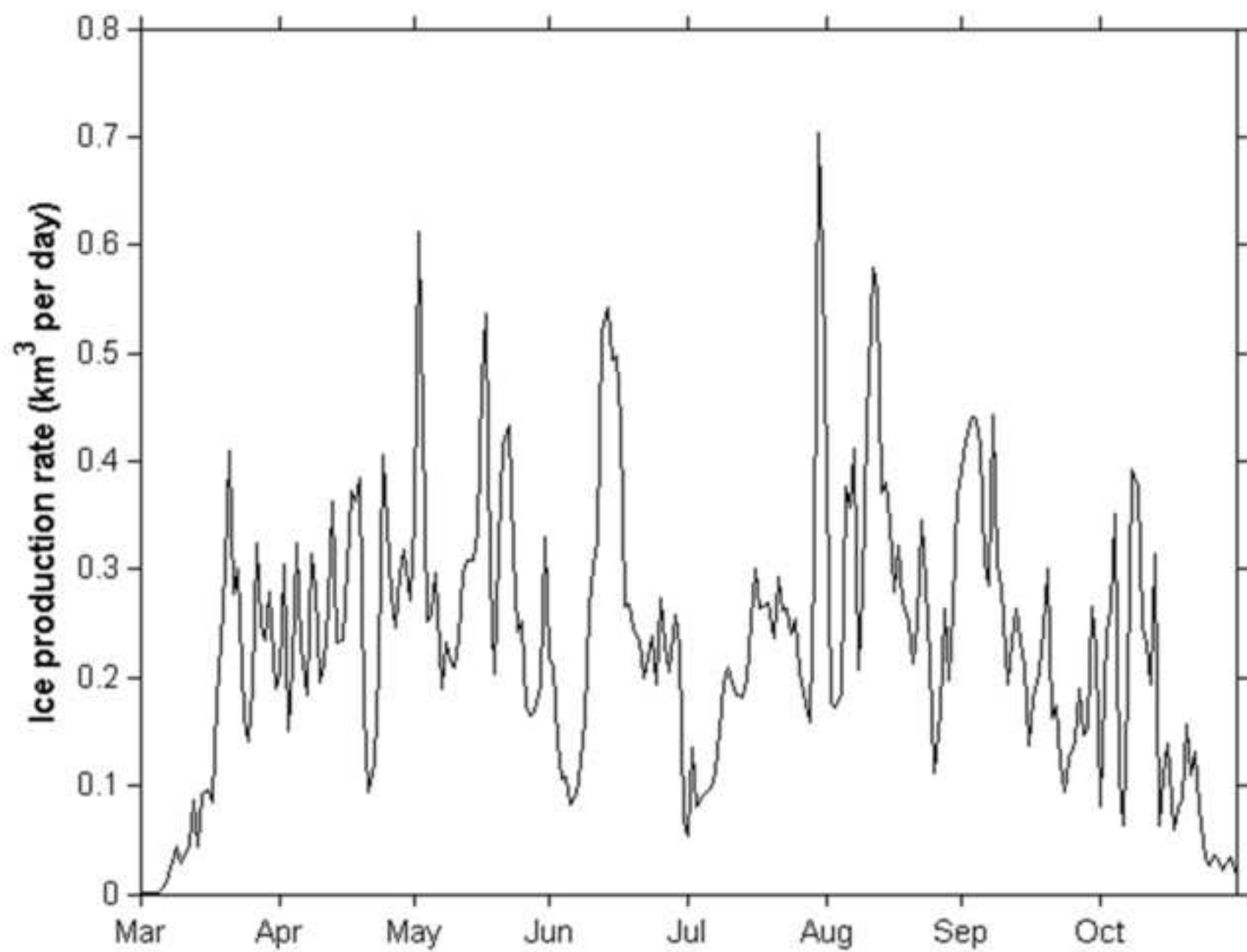


Figure(s)
[Click here to download high resolution image](#)



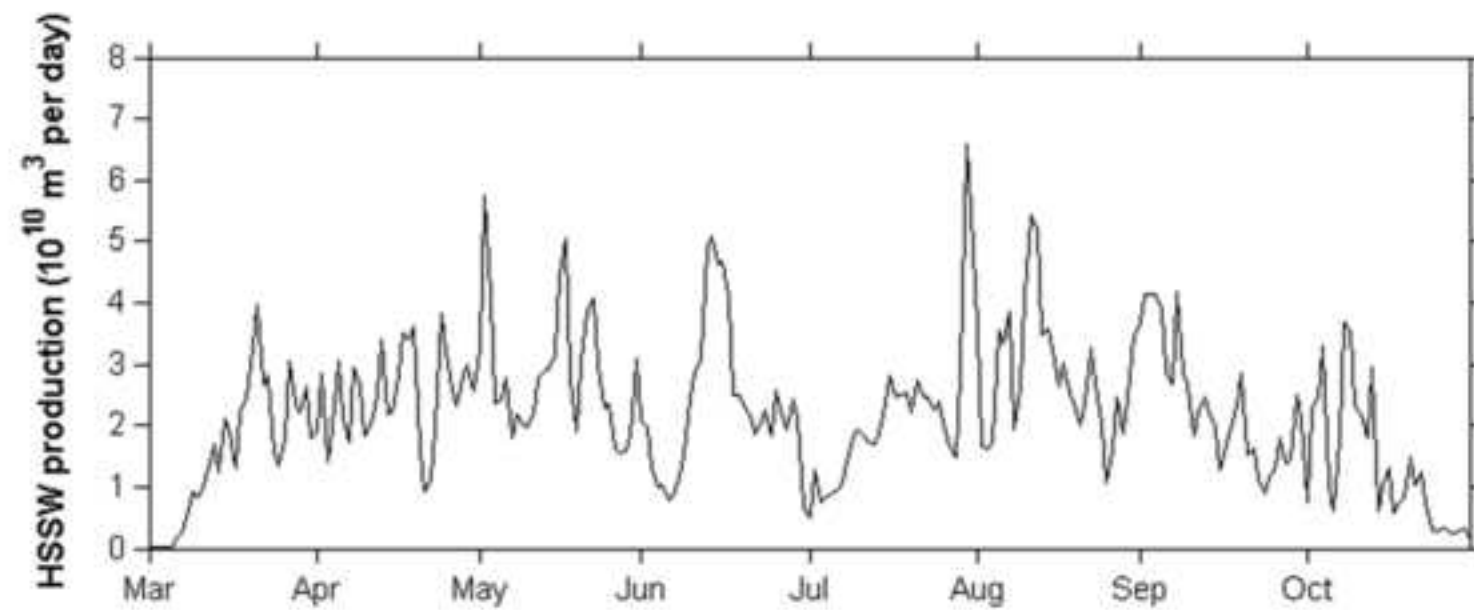
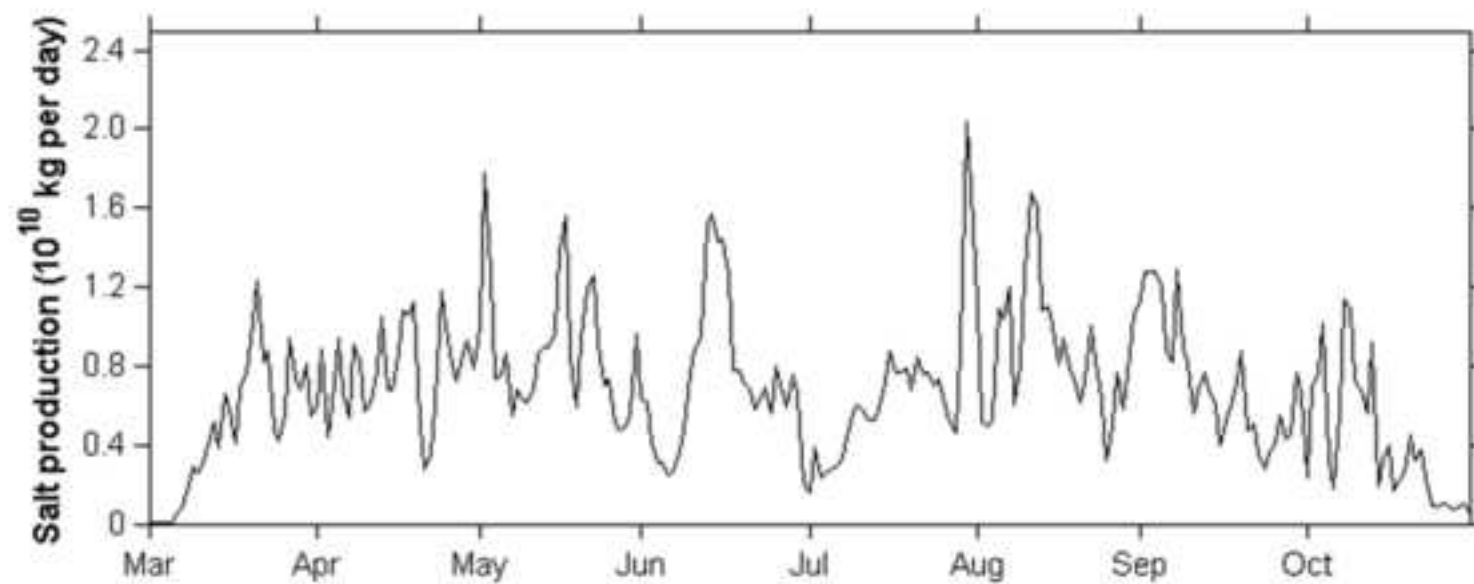
Figure(s)

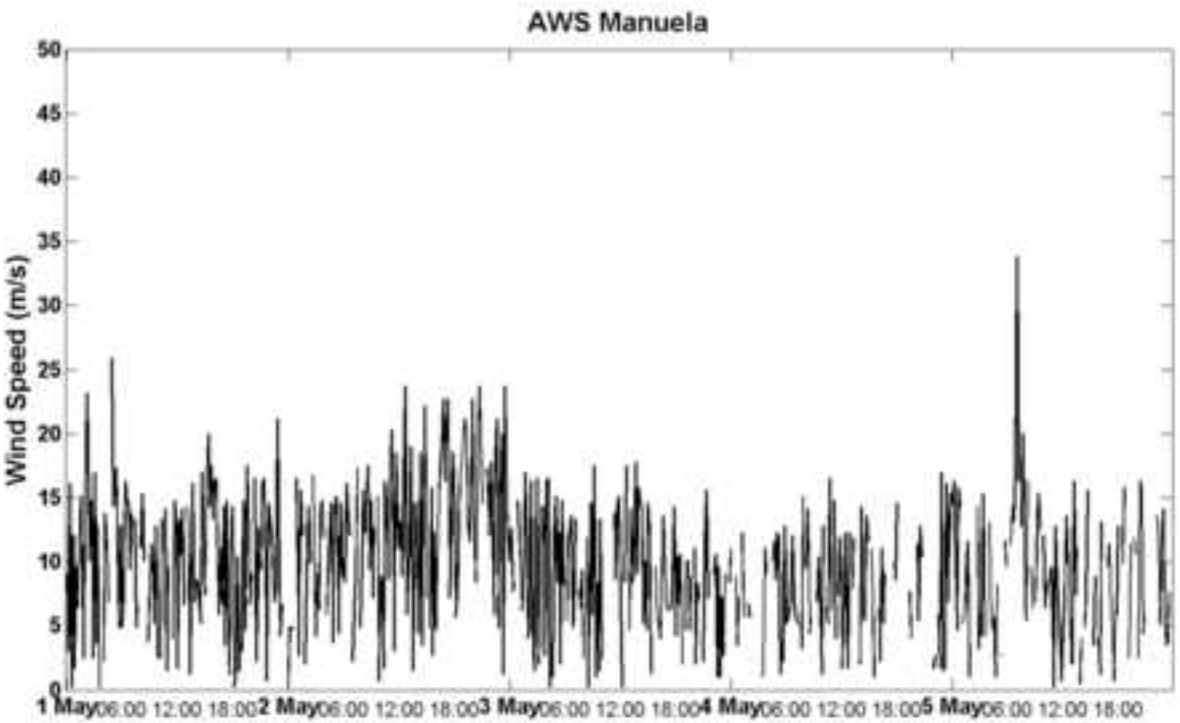
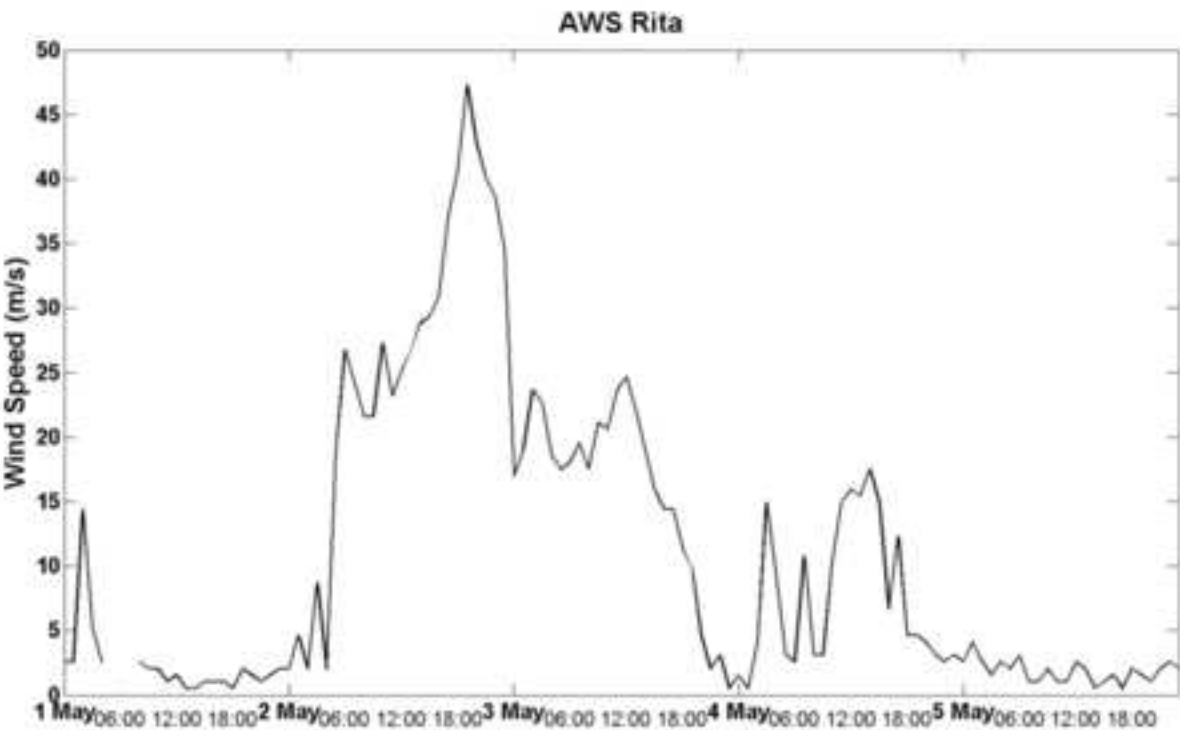
[Click here to download high resolution image](#)



Figure(s)

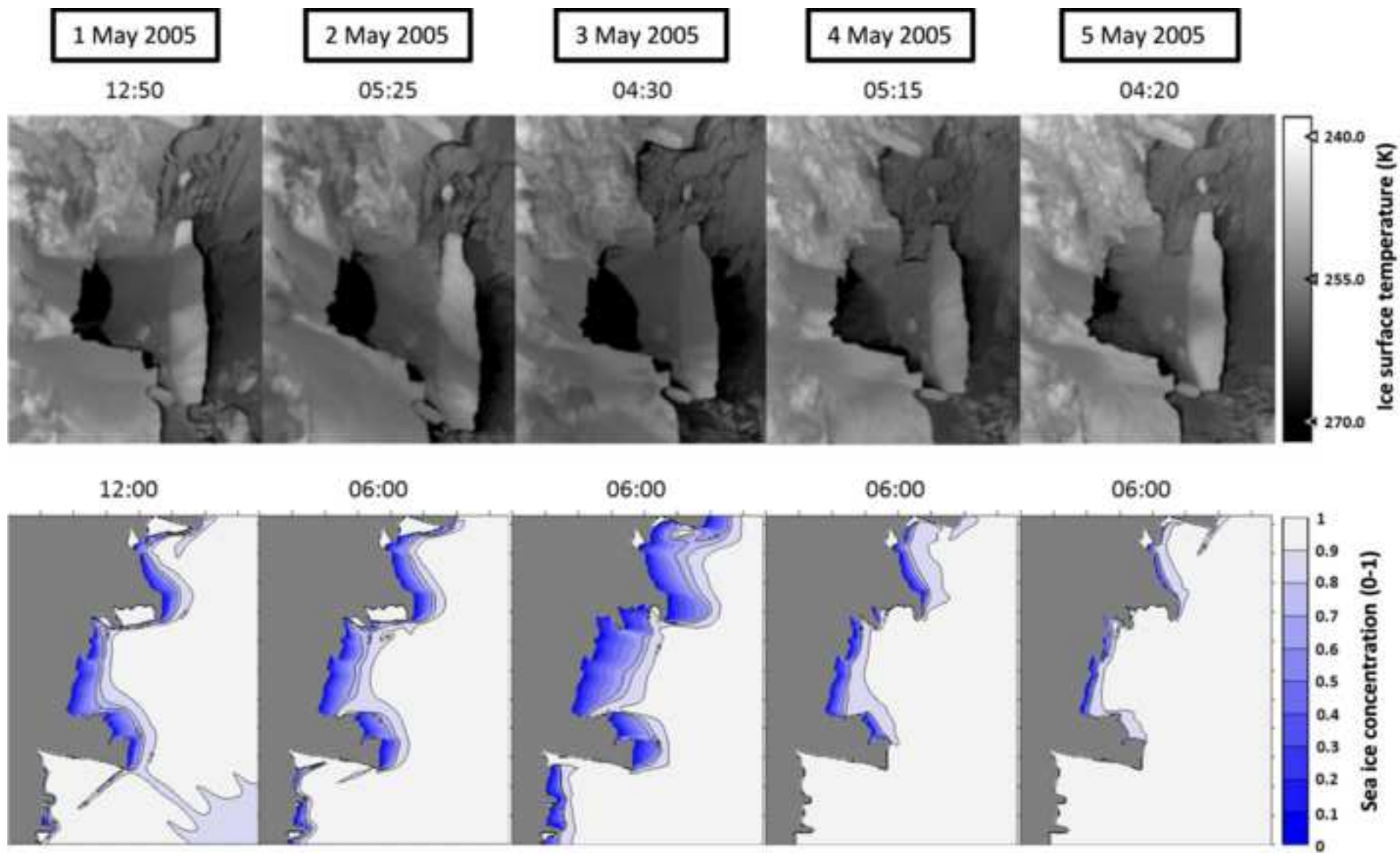
[Click here to download high resolution image](#)

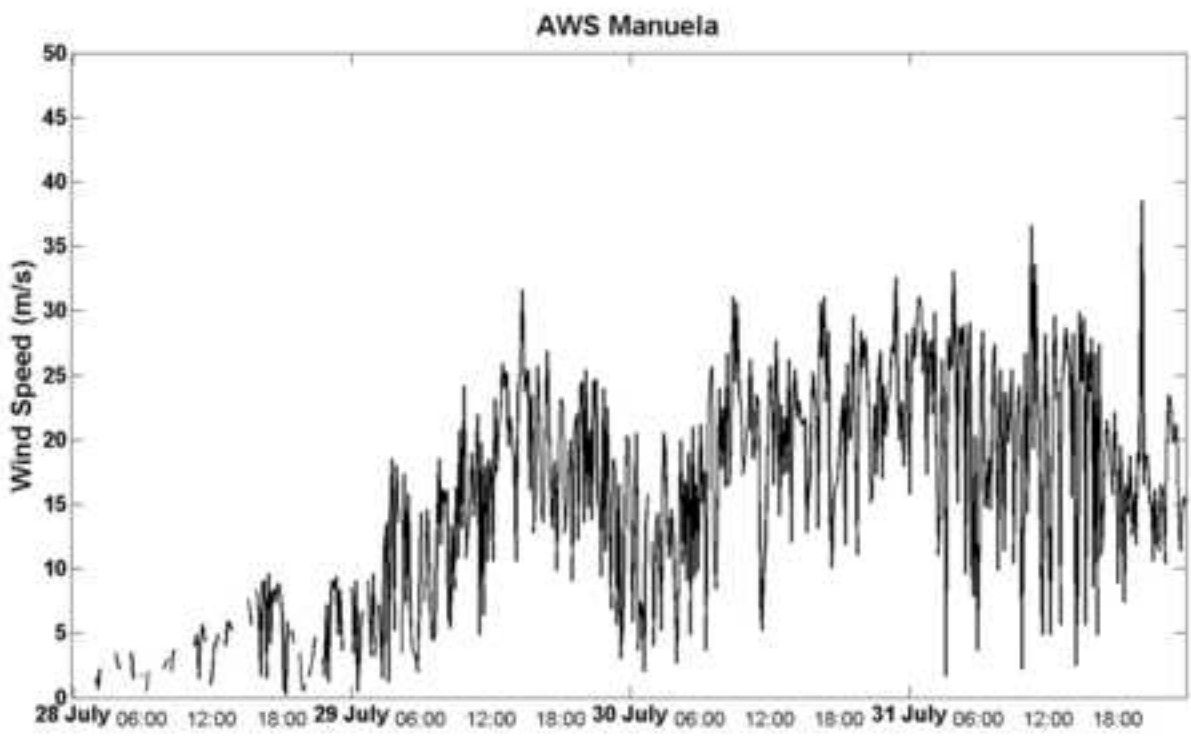




Figure(s)

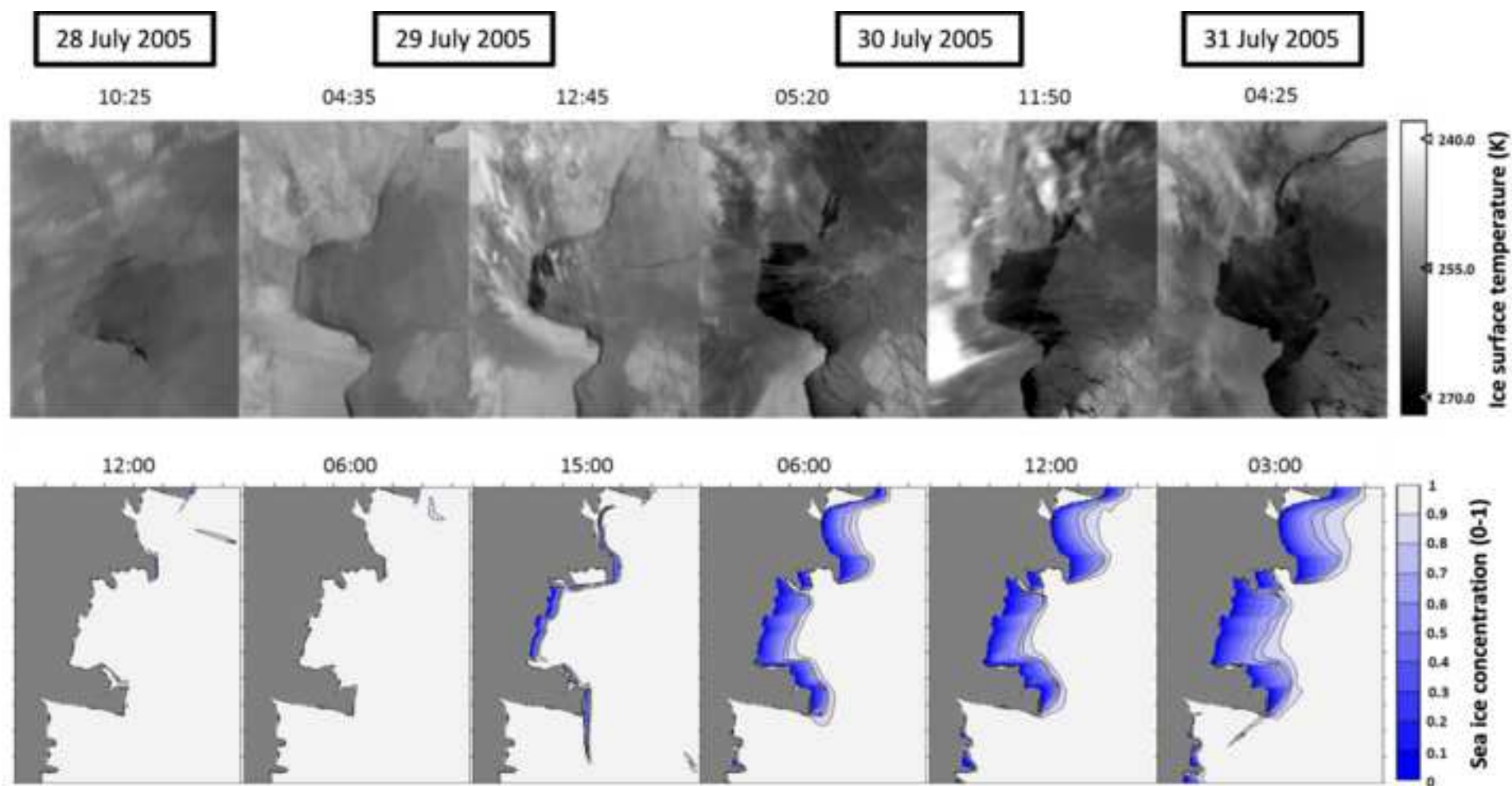
[Click here to download high resolution image](#)





Figure(s)

[Click here to download high resolution image](#)



Parameter	Symbol	Value
X domain	X	154000 m
Y domain	Y	488000 m
T domain	T	x days
Time step for momentum	Δt	1.2 s
Time step for advection	Δt_a	600 s
Elastic timescale (EVP ice rheology)	Δt_e	180 s
Air drag coefficient	C_{da}	x
Ocean drag coefficient	C_{do}	x
Ice strength parameter	P^*	x N/m ²
Ice concentration parameter	C	20
Creep limit	c	5×10^{-11} 1/s
Eccentricity of the elliptical yield curve	e	2
Ice collection thickness in leads	H	x m

Table 1: Input parameters of the model. The “x” stands for a varying value assigned to that parameter in the sensitivity experiments.

Parameter	Symbol	Value
Ocean eddy thickness diffusivity	κ_e	$2 \times 10^2 \text{ m}^2 \text{ s}^{-1}$
Thermal conductivity of sea ice	κ_i	2.2 W/m/K
Thermal conductivity of snow	κ_s	0.3 W/m/K
Emissivity of atmosphere	ε_a	0.95
Emissivity of ocean	ε_o	0.985
Albedo of ocean	α_o	0.07
Albedo of ice	α_i	0.07-0.7
Albedo of snow	α_{sn}	0.85
Latent heat of fusion of ice	L_{fi}	$3.34 \times 10^5 \text{ J/kg}$
Latent heat of vaporization of water	L_e	$2.5 \times 10^6 \text{ J/kg}$
Latent heat of fusion of snow	L_{fsn}	$3.34 \times 10^5 \text{ J/kg}$
Latent heat of sublimation of snow	L_{ssn}	$2.834 \times 10^6 \text{ J/kg}$
Specific heat capacity of ocean	c_{pa}	3985 J/kg/K
Specific heat capacity of air	c_{pa}	1004 J/kg/K
Density of air	ρ_a	1.3 Kg/m ³
Density of ice	ρ_i	900 Kg/m ³
Density of snow	ρ_s	330 Kg/m ³
Density of ocean	ρ_o	1024 Kg/m ³
Melting point of freshwater ice	t_{fus}	0°C
Salinity of sea ice	s_i	4
Exchange coeff. for sensible heat (leads/ice)	c_H	1.75×10^{-3}
Exchange coeff. for latent heat over leads	c_E	1.75×10^{-3}
Exchange coeff. for latent heat over ice	c_E	1×10^{-3}
Stefan-Boltzmann constant	K	$5.67 \times 10^{-8} \text{ W m}^{-2} \text{ K}^{-4}$
Minimum vertical viscosity	ν_{min}	$1 \times 10^{-3} \text{ m}^2 \text{ s}^{-1}$
Scale depth of mechanical dissipation	h_w	7 m
Scale depth of convective dissipation	h_c	50 m

Table 2: Physical parameters of atmosphere, sea ice and ocean.

Table(s)
[Click here to download Table\(s\): Table 3.docx](#)

Experiment	P^* (N/m ²)	R (km)
CASE 1	27500	25
CASE 2	5000	25
CASE 3	27500	-
CASE 4	27500	50

Table3: Sensitivity tests of sea ice evolution with respect to P^* and R factor.

Experiment	<i>H</i> (m)	R factor (km)
CASE 5	0.2	50
CASE 6	0.3	50
CASE 7	0.4	50
CASE 8	<i>f</i> (V)	50
CASE 9	0.2	-

Table 4: Sensitivity tests of sea ice evolution with respect to *H* and *R* factor.

Experiment	Sea ice production (km ³) in July 2000
CASE 5	10.08
CASE 6	11.09
CASE 7	12.12
CASE 8	9.79
CASE 9	6.83

Table 5: Sea ice production in July 2000 for the experiments CASE 5 to CASE 9.

Experiment	C_{da}	C_{do}
E ₁₅ <u>CTRL</u>	1×10^{-3}	5×10^{-3}
E ₃₅	3×10^{-3}	5×10^{-3}
E ₁₁	1×10^{-3}	1×10^{-3}
E ₃₁	3×10^{-3}	1×10^{-3}
E ₃₄	3×10^{-3}	4×10^{-3}
E _r	1×10^{-3} $V \leq 10$ m/s 3×10^{-3} $V \geq 20$ m/s	$1.3 \times C_{da}$

Table 6: Sensitivity tests with respect to the air-ice and ice-ocean drag coefficients. The double sub-index identifies the wind and ocean drag coefficients used in each experiment.

Winter months	Maximum Polynya extent (km ²)	Mean Polynya extent (km ²)
March	7946	5574
April	1806	1174
May	2688	871.2
June	2205	557.2
July	2962	532.5
August	2868	766.9
September	2674	875.6
October	5637	2304

Table 7: Monthly maximum and mean polynya extent of the TNB polynya from March to October 2005.

Winter months	Maximum daily rates of sea ice production (km ³ /day)	Mean daily rates of sea ice production (km ³ /day)	Monthly cumulative sea ice (km ³)
March	0.42	0.16	4.99
April	0.40	0.26	7.86
May	0.61	0.30	9.25
June	0.54	0.25	7.52
July	0.70	0.22	6.98
August	0.58	0.30	9.39
September	0.44	0.24	7.34
October	0.39	0.14	4.29

Table 8: Daily sea ice production rates from spatially cumulated ice production in TNB polynya region from March to October 2005.

TNB polynya event in July 2005	Model-derived polynya extent (km ²)	MODIS-derived polynya extent (km ²)
28 th 12:00	12	40
29 th 06:00	0	25
29 th 15:00	389	391
30 th 06:00	1858	1936
30 th 12:00	2148	2385
31 th 03:00	2831	3393

Table 9: TNB polynya extents from model sea ice concentration outputs and from MODIS IST from 28th to 31th July 2005.